Subcutaneous nanotherapy repurposes the immunosuppressive mechanism of rapamycin to enhance allogeneic islet graft viability

Authors: Jacqueline A. Burke[1,2], Xiaomin Zhang[3], Sharan Kumar Reddy Bobbala[1], Molly A. Frey[3,4], Carolina Bohorquez Fuentes[1,2], Helena Freire Haddad[1,2], Sean D. Allen[4], Reese A.K. Richardson[4], Luís A. Nues Amaral[4,5], Guillermo A. Ameer[1,2,3,4,5,6,7]*, Evan A. Scott[1,2,4,5,6,7]*

Author Affiliations:

1. Department of Biomedical, Northwestern University, 2145 Sheridan Road, E311, Evanston, IL 60208;
2. Center for Advanced Regenerative Engineering, Northwestern University, 2145 Sheridan Road, E311, Evanston, IL 60208;
3. Feinberg School of Medicine, Northwestern University, 420 E. Superior Street, Chicago, IL 60611;
4. Interdisciplinary Biological Sciences, Northwestern University, 2205 Tech Drive, Evanston, IL 60208;
5. Department of Chemical and Biological Engineering, Northwestern University, 2145 Sheridan Road, E361, Evanston, IL 60208;
6. Simpson Querrey Institute, Northwestern University, 303 E. Superior Street, 11th Floor, Chicago, IL 60611;
7. International Institute for Nanotechnology, Northwestern University, 2145 Sheridan Road, K111, Evanston, IL 60208

Co-Corresponding Authors:

Evan A. Scott, Ph.D.
Department of Biomedical Engineering
Northwestern University
2145 Sheridan Road Silverman Hall 4613
Evanston, IL 60208
Phone: 847-467-6719
E-mail: evan.scott@northwestern.edu

Guillermo A. Ameer, Sc.D.
Department of Biomedical Engineering
Northwestern University
2145 Sheridan Road B382
Evanston, IL 60208
Phone: 847-491-4928
E-mail: g-ameer@northwestern.edu

Keywords: Rapamycin; Nanocarrier; Immunosuppression; Immunomodulation; Costimulation Blockade; Islets Transplantation; Type I Diabetes; Drug Delivery; Nanomedicine; Subcutaneous Delivery

Abstract

Rapamycin is an orally administered immunosuppressant that is plagued by poor bioavailability and a wide biodistribution. Thus, this pleotropic mTOR inhibitor has a narrow therapeutic window, a wide range of side effects and provides inadequate transplantation protection. Here, we demonstrate that subcutaneous rapamycin delivery via poly(ethylene glycol)-*b*-poly(propylene sulfide)) (PEG-*b*-PPS) polymersome (PS) nanocarriers modulates the cellular biodistribution of rapamycin to change its immunosuppressive mechanism of action for enhanced efficacy while minimizing side effects. While oral rapamycin inhibits naïve T cell proliferation directly, subcutaneously administered rapamycin-loaded polymersomes (rPS) instead modulated Ly-6C^{low} monocytes and tolerogenic semi-mature dendritic cells, with immunosuppression mediated by CD8+ Tregs and rare CD4+CD8+ double-positive T cells. As PEG-*b*-PPS PS are uniquely non-inflammatory, background immunostimulation from the vehicle was avoided, allowing immunomodulation to be primarily attributed to rapamycin's cellular biodistribution. Repurposing mTOR inhibition significantly improved maintenance of normoglycemia in a clinically relevant, MHC-mismatched, allogeneic, intraportal (liver) islet transplantation model. These results demonstrate the ability of engineered nanocarriers to repurpose drugs for alternate routes of administration by rationally controlling cellular biodistribution.

Introduction

Type 1 diabetes (**T1D**) is an endocrine disorder that leads to pancreatic β cell destruction and requires management by lifelong exogenous insulin therapy.[1,2] With the advent of the Edmonton protocol, islet transplantation has emerged as a promising treatment for T1D by eliminating the need for exogenous insulin. This protocol involves three key components: acquisition of viable insulin-producing cells, surgical transplantation of these cells into a suitable physiological location to maintain glucose sensitivity and responsiveness, and an immunosuppressive regimen to maintain islet viability and protection from the host immune system [3,4]. While all three components remain active areas of research, the need for immunosuppression remains the key limitation preventing islet transplantation from becoming the clinical standard of care for all T1D patients.[5] [3,4]. A critical advancement in this regard was the advent of orally administered nanocrystal rapamycin, i.e Rapamune, for non-steroidal immunosuppressive protocols. Rapamycin inhibits the mammalian target of rapamycin (**mTOR**) pathway to directly inhibit T cell proliferation by arresting these cells in the G1 phase of the cell cycle and preventing IL-2 secretion[6,7]. Although more effective than prior immunosuppressive protocols involving intravenous steroid administration, patients undergoing transplantation procedures are still plagued by frequent graft rejection and an unpleasant array of side effects[8].

Side effects related to oral rapamycin administration stem primarily from poor and inconsistent bioavailability and the wide cellular biodistribution. Rapamune has a bioavailability of only 14% in the solution form and 41% in tablet form[9]. The low bioavailability is attributed primarily to the first pass metabolism associated with the oral route of administration, cytochrome P450 elimination and transport by p-glycoprotein efflux pumps[10]. For example, absorption of Rapamune is greatly varied by fat content in food[9], and cytochrome P450 isoenzyme CYP3A4 metabolism can cause serious drug-drug interactions[10]. With regards to biodistribution, lipophilic Rapamune primarily partitions into red blood cells (95%) and then eventually accumulates in off-target organs, including the heart, kidneys, intestines and testes[11-14], leading to side effects. These side effect occur due to the ubiquitous expression of mTOR in diverse cell types, resulting in unintended cell populations also experiencing cell cycle arrest [6,7]. Clinically, this leads to malignancy, enhanced susceptibility to infection, impaired wound healing, thrombopenia, alopecia, gastrointestinal distress gonadal dysfunction, hypertension, hyperlipidemia, nephrotoxicity and peripheral edema[6,15]. In order to balance the need to maintain immunosuppression with the

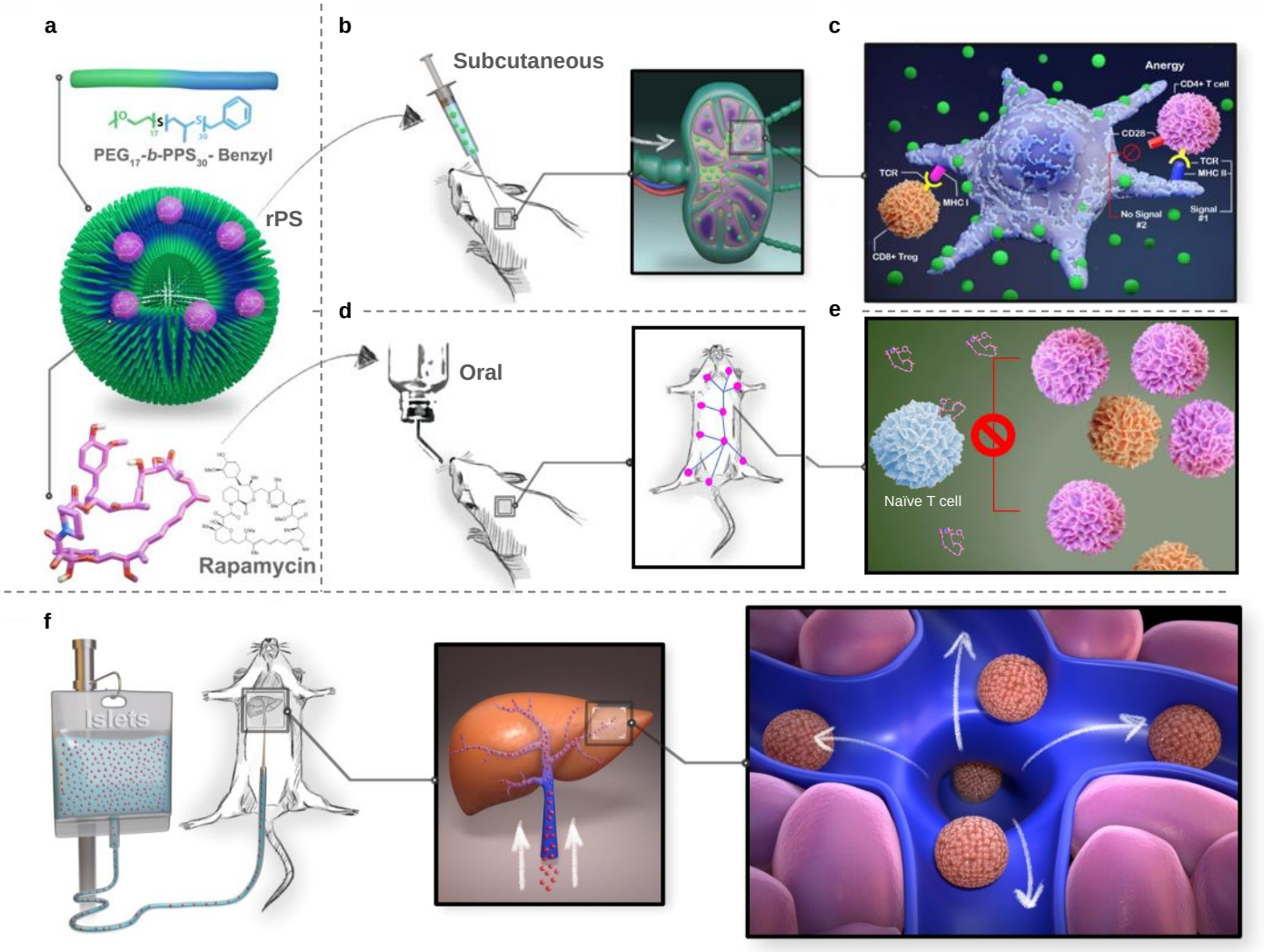

Fig. 1 | Subcutaneous rapamycin delivery to APCs via rPS signals T cells to tolerate fully-MHC mismatched intraportal islet graft. a, Rapamycin can be easily loaded into the hydrophobic membrane of PS to form rPS. **b,** When injected subcutaneously into mice, rPS drain into the brachial lymph nodes where they are uptaken by APCs. **c,** As a result, APCs develop an anti-inflammatory, semi-mature phenotype, in which they express high levels of MHC II to present to CD4+ T cell receptors, but they do not express costimulatory molecules, thus preventing costimulation. Without activation, acute rejection causing CD4+ T cells go into a state of anergy or become tolerogenic CD8+ Tregs **d,** Clinically, rapamycin is given orally. Oral administration results in a wide biodistribution and low bioavailability. **e,** Oral rapamycin primarily acts on T cells directly by inhibiting mTOR and thus preventing T cell proliferation. **f,** To assess the ability of subcutaneous rPS to provide a tolerogenic state that allows for fully-MHC mismatched allogeneic graft survival, islet transplantation was performed in diabetic mice at the clinically relevant intraportal (liver) transplantation site and graft viability was assessed by the restoration and maintenance of normoglycemia.

avoidance of side effects, patients must undergo frequent blood work to ensure that the rapamycin concentration is within the small therapeutic window of 5 to 15 ng/ml[10]. Of note, mTOR inhibition can have distinct responses depending on the cell type. For example, rapamycin retains dendritic cells (**DCs**) in an immature tolerogenic state that resists coreceptor expression in response to inflammatory stimuli, a process known as costimulation blockade.

Given the plethora of problems associated with oral Rapamune, an alternative therapy that bypasses the oral route of administration, reduces adverse effects, and enhances transplantation outcomes is needed. Subcutaneous administration would avoid bioavailability issues that plague Rapamune including first pass metabolism, elimination by intestinal cytochrome P450 and p-glycoprotein, and variability associated with food content. Importantly, the subcutaneous route of administration provides the advantage of targeting lymphatic drainage[16]. Unlike intravenous administration, the subcutaneous route allows patients to take their medication from their own home. Furthermore, the T1D patient population is well versed in the subcutaneous method of injection due to the need to inject insulin. However, due to the lipophilic nature of rapamycin (log P 4.3), it is poorly soluble and therefore very difficult to formulate into a parental drug for subcutaneous administration[17]. Additionally, subcutaneous administration of rapamycin is unlikely to achieve the required biodistribution to directly inhibit T cell proliferation and prevent islet rejection. But the subcutaneous route does provide access to antigen presenting cells (**APCs**), including the aforementioned DCs that can elicit potent tolerogenic responses upon modulation by rapamycin. Tolerogenic DCs (**tDCs**) constitutively generate regulatory T cells (**Tregs**) as well as express anti-inflammatory cytokines, both of which have been linked to enhanced survival of transplanted islets[16].

We hypothesized that focusing rapamycin's mTOR inhibition on APCs using engineered nanocarriers could achieve sustained immunosuppression and survival of transplanted islets via the subcutaneous route with lower dosage and minimal side effects (**Fig. 1**). To focus the broad biodistribution of rapamycin specifically to APCs, we generated rapamycin-loaded poly(ethylene glycol)-*b*-poly(propylene sulfide)) (**PEG-*b*-PPS**) polymersomes (**rPS**). The PEG-*b*-PPS polymersome (**PS**) platform allows for efficient loading of lipophilic drugs within the PPS membrane[18], has been validated to be nontoxic in both mice and nonhuman primates [19-22] and undergoes uptake by DC and monocyte populations[23], which are critically responsible for directing T cell activation during immune responses[21,24,25]. Importantly, PEG-*b*-PPS is non-immunomodulatory relative to other common nanomaterials,

with an immunostimulatory profile that is determined almost exclusively by the loaded therapeutic[23]. Unloaded PEG-*b*-PPS PS elicit minimal immunomodulatory activity, whereas comparable poly(lactic-co-glycolic acid) (**PLGA**) nanocarriers cause an extensive immunomodulatory response, including alteration of immune cell

populations[26], changes in coreceptor expression (e.g. CD80, CD86)[27], and modification the inflammatory status of specific immune cell populations[27]. Thus, our mechanistic assessment of rPS-mediated immunosuppression avoids interference from background immunomodulation by the drug vehicle itself.

To the best of our knowledge, herein we present the first therapeutic application of subcutaneous rapamycin nanotherapy, as well as the first reorchestrating of the immunological mechanism of an immunosuppressant by rationally selecting its cellular biodistribution. Efficacy of this strategy is assessed via high parameter spectral flow cytometry with analysis via T-distributed stochastic neighbor embedding (**tSNE**), single-cell RNA sequencing and a clinically relevant intraportal fully-major histocompatibility complex (**MHC**) mismatched allogeneic islet transplantation model. Our results reveal the mechanisms behind how nanocarrier-mediated modulation of cellular biodistribution can significantly change the therapeutic window, reduce adverse events, and enhance anti-inflammatory efficacy of an immunosuppressant by rationally changing its therapeutic mechanism of action.

Results

Morphological characterization of rPS

PEG-*b*-PPS PS were characterized to assess encapsulation efficiency and retention of their vesicular nanostructure following the loading of rapamycin to form rPS. Rapamycin encapsulation efficiency was found to

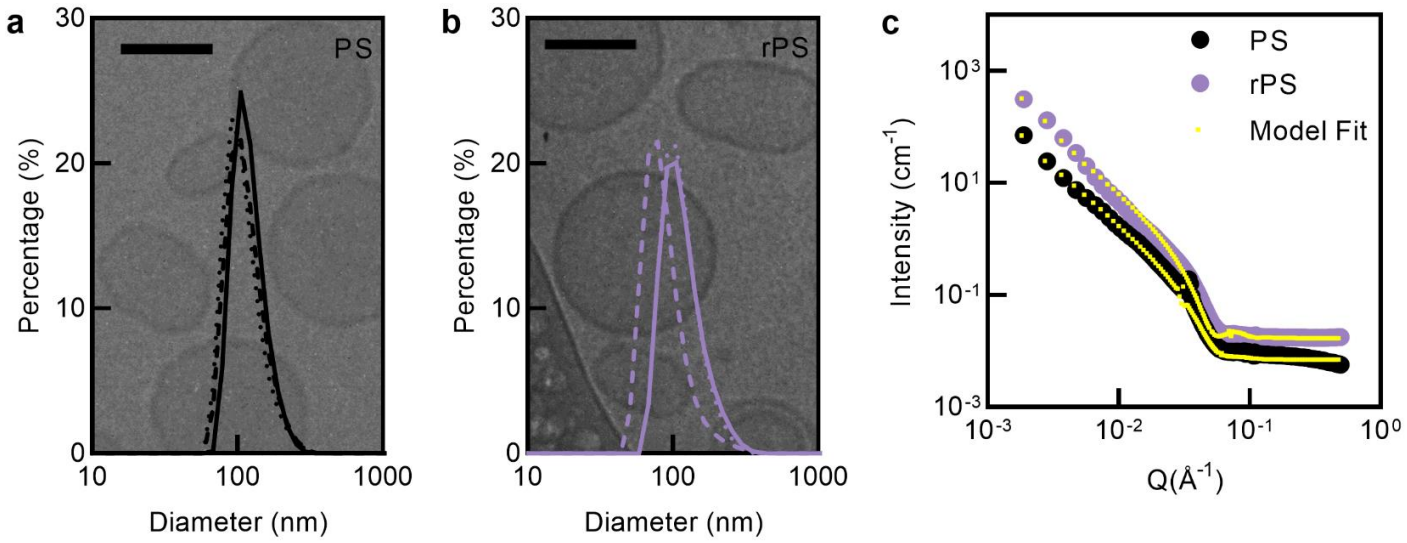

Fig. 2 | Morphological characterization of PS and rPS. a,b, cryoTEM of PS (**a**) and rPS (**b**) with overlay of size distribution by DLS (n = 3). Scale bars represent 100 nm. (n = 3). **c,** SAXS transformed data of PS (●) and rPS (●) with polymer vesicular model fit (--). (n = 3-5).

be greater than 55% for rPS following self-assembly and therapeutic loading via thin film hydration of desiccated PEG-*b*-PPS films. Neither the PS vesicular nanostructure nor the polydispersity were significantly modulated by rapamycin loading as assessed by dynamic light scattering (**DLS**), cryogenic transmission electron micrograph (**cryoTEM**) and small angle x-ray scattering (**SAXS**) (**Fig. 2a-c**). The stability of rapamycin loading was assessed in PBS at 4 °C, finding approximately 94% of the drug was retained over the course of 1 month (**Fig. S1**). Rapamycin is relatively lipophilic with a logP of 4.3[28], and thus these results were consistent with past attempts to load molecules of low water solubility into PEG-*b*-PPS nanostructures.

Subcutaneous PS delivery alters organ and cellular biodistribution and immunomodulation.

To demonstrate that PEG-*b*-PPS PS can alter the biodistribution of a traceable small molecule following subcutaneous, indocyanine green dye (**ICG-PS**) was loaded into PS to serve as a model payload. We subcutaneously injected C57BL/6J mice with ICG-PS or free ICG, sacrificed animals at 2, 24, and 48 h post injection and analyzed organs via IVIS (**Fig. S2**). We show that ICG-PS allowed for sustained residence within to the brachial lymph nodes at 24 and 48 h post-injection, whereas free form ICG dye had been cleared at these later time points (**Fig. 3a**). To confirm that this effect holds true for rapamycin, rapamycin (in 0.2% carboxymethyl cellulose (**CMC**)) or rPS were subcutaneously injected into C57BL/6J mice and the animals were sacrificed at 0.5, 2, 8, 18, 24, and 48 h post-injection to assess rapamycin content in various organs. We showed that delivery of rapamycin via rPS increases rapamycin concentration in immune cell-rich tissues, such as the blood, liver, draining axial and brachial lymph nodes and spleen (**Fig. 3b**). To assess both the organ and cellular effects of rapamycin delivery via PEG-*b*-PPS PS, immune cell populations from various tissues were isolated after repeated subcutaneous injection with unloaded PS, rapamycin or rPS formulations (**Fig. 3c**). When unloaded PS were injected, very little immunomodulation was observed (**Fig. 3c**). However, when rapamycin was loaded with in the PS, potent immunomodulation occurred (**Fig. 3c**). The relative immunologically inert status of the unloaded PS allowed for the majority of the effects of rPS to be attributed to the altered biodistribution of the drug, as opposed to the nanocarrier itself. A significant change in immunomodulation is observed when rPS is given as compared to rapamycin on its own (**Fig. 3c**). Taken in combination with the inert nature of PEG-*b*-PPS,

our results suggested that a drug's organ and cellular biodistribution have a strong influence on the resulting immunological effect.

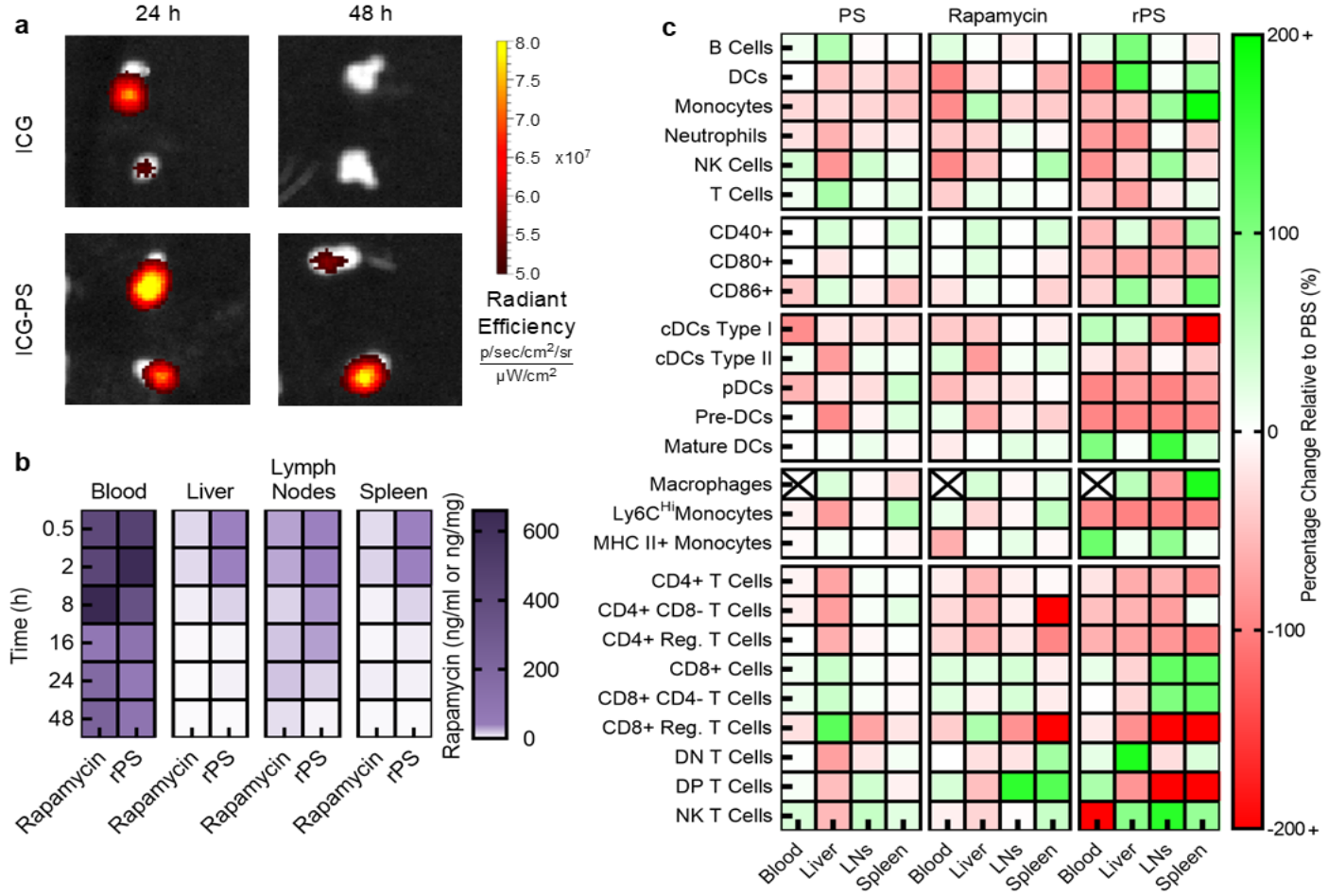

Fig. 3 | Subcutaneous PS delivery alters organ and cellular biodistribution and immunomodulation. a, Biodistribution of indocyanine green (ICG) dye by formulation in the brachial lymph nodes 24 and 28 h after subcutaneous injection (n = 5 mice). **b,** Biodistribution of rapamycin by formulation. Rapamycin concentration in the blood, liver, axial and brachial lymph nodes, and spleen over time (0.5 h, 2 h, 8 h, 16 h, 24 h and 48 h) as assess by LC-MS/MS. (n = 3 mice). **c,** Flow cytometry analysis of mice subcutaneously injected with PBS, PS, rapamycin (in 0.2% CMC), or rPS for 11 days at a dose of 1 mg/kg/day rapamycin or equivalent. Macrophages were not assessed in blood as indicated by a black "X" in a white box. All data are presented as mean percentage change relative to PBS treatment. (n = 3 mice).

Altered rapamycin biodistribution via subcutaneous rPS delivery changes immune cell populations in multiple organs.

To more deeply characterize changes in immune cell populations in response to rPS delivery, we subcutaneously injected healthy mice with PBS, unloaded blank PS, rapamycin, or rPS (11 injections, 1 mg/kg rapamycin or equivalent) and subsequently extracted a variety of organs for assessment via high-parameter spectral flow cytometry. tSNE with Barnes-Hut approximations was used to visualize the data after gating (**Fig.**

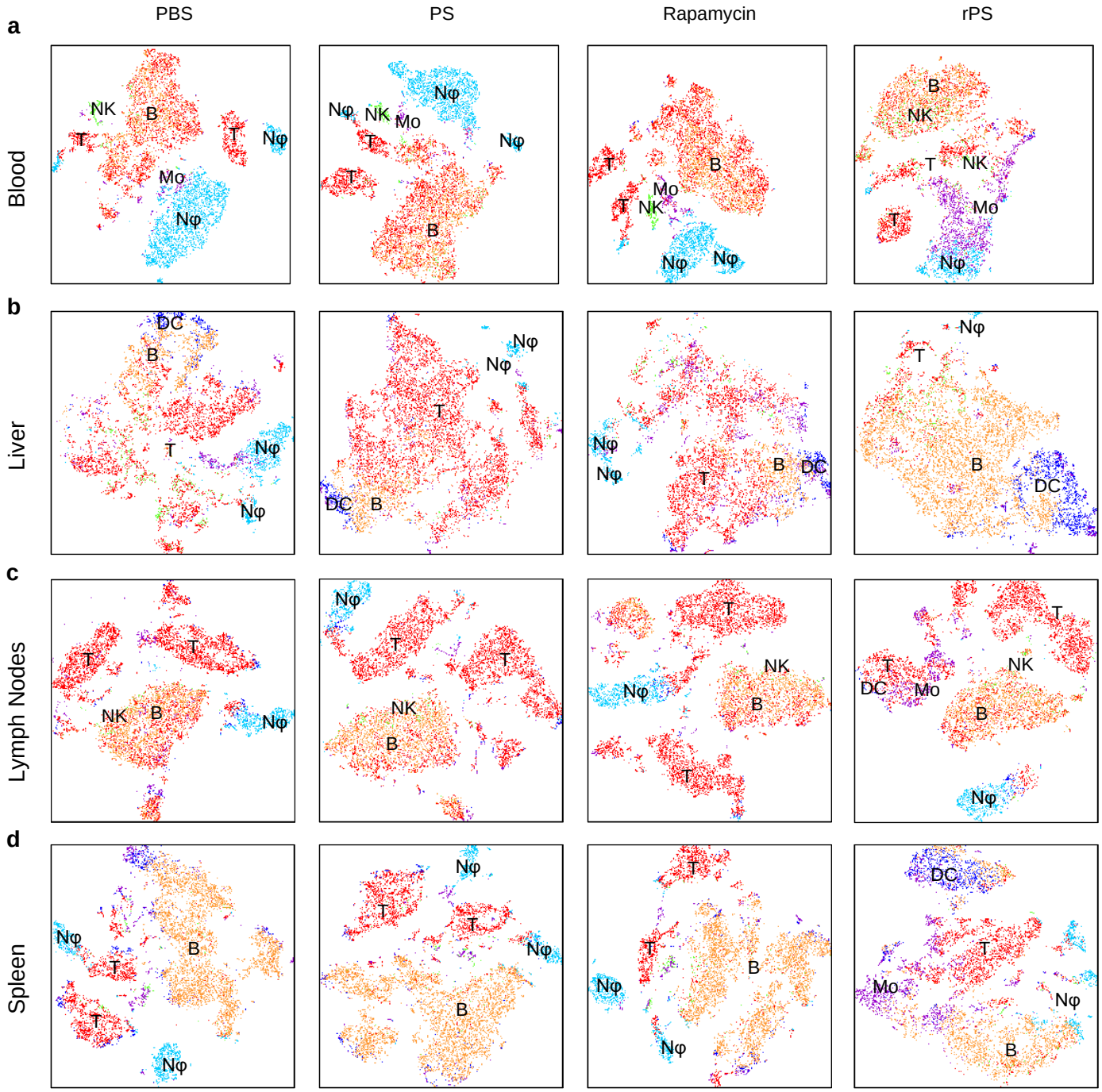

Fig. 4 | Altered rapamycin biodistribution via subcutaneous rPS delivery modifies immune cell populations. Mice were injected subcutaneously with PBS, PS, rapamycin or rPS using the standard dosage protocol (11 injections, 1 mg/kg rapamycin or equivalent). Cell populations were analyzed by flow cytometry. (n = 3 mice). tSNE visualization of CD45+ cells from blood (**a**), liver (**b**), axial and brachial draining lymph nodes (**c**) and spleen (**d**). Color- coded gated overlays include B cells (B; orange), DCs (DC; blue), monocyte linage cells (CD11b+) (Mo; purple), neutrophils (Nφ; light blue), and T cells (T; red).

S4), down sampling and concatenation of treatment groups. Cell populations were visualized via tSNE with hand-gated overlays distinguished by color. In blood, several distinct cell populations were observed: B cells, monocytes, natural killer (**NK**) cells, neutrophils, and T cells (**Fig. 4a, S5**). With rPS treatment, the NK cell population was significantly larger, and the monocyte population trended towards an increase in size (**Fig. 4a,**

S5a). Two neutrophil clusters (CD11b^{Mid} and CD11b^{Hi}) and two T cell clusters were seen (CD4+ and CD8+) (**Fig. 4a, S5b-e**). However, with rPS treatment there was only one neutrophil cluster with CD11b^{Mid} expression (**Fig. 4a, S5b,c**), thus the size of the neutrophil population was significantly reduced relative to PBS treatment (**Fig. 5a**). While with rPS treatment, two T cell clusters remained; CD4+ T cells had reduced expression levels of CD4 (**Fig. S5c**), while CD8+ T cells had a more diverse range of phenotypes as indicated by the wide spread of the CD8+ T cell cluster (**Fig. S5b,d**).

In the liver, generally, less distinct clustering of cells was observed (**Fig. 4b**). Commonly, a large T cell population dominated (**Fig. 4b, S6a**). Distinct CD4+ and CD8+ T cell clustering was not observed (**Fig. 4b, S6c,d**). Clustering was absent because the CD8+ T cell population was predominate over CD4+ T cells (**S6c,d**). Regardless, with rPS treatment, the overall T cell population was significantly decreased. (**Fig. 4b, S6a**). Outer clusters of B cells, DCs, and neutrophils were observed for all treatments (**Fig. 4b**). With rPS treatment, the B cell population significantly increases, while the neutrophil population was significantly reduced (**Fig. 4b, S6a**). Similar to blood, generally there were two neutrophil populations CD11b^{Lo} and CD11b^{Hi} (**Fig. S6b,c**). However, with rPS treatment, there is only a single neutrophil population with neutral CD11b expression (**Fig. S6b,c**).
In the draining axial and brachial lymph nodes, similar cell clustering to that in blood was observed (**Fig. 4a,c**). However, only a single population of CD11b^{Lo} neutrophils exists for each treatment (**Fig. 4c, S7b-d**). Distinct CD4+ and CD8+ T cell populations were present (**Fig. 4c, S7b-d**). Following rPS treatment, the CD4+ T cell population was reduced, and significant upregulation of monocytes and DC populations occurred (**Fig. 4c, S7a-c**). Furthermore, the CD4+ T cell populations shows reduced CD4 expression with rPS treatment (**Fig. S7c**). In contrast, the CD8+ T cell cluster was significantly enlarged with rPS treatment (**Fig. S7d**). Overall, significantly fewer T cells were observed for the rPS treated group (**Fig. 4c, S7a**). In the non-draining inguinal lymph nodes, cell clustering was very similar to the draining lymph nodes with the addition of significant increases in neutrophils and NK cells (**Fig. S8**).

In the spleen, generally, we saw a large B cell population accompanied by two smaller neutrophil clusters—CD11b^{Lo} and CD11b^{Hi} and two smaller T cell clusters—CD4+ and CD8+ (**Fig. 4d, S9b-e**). Minute DC and monocyte populations were also visible (**Fig. 4d**). However, with rPS treatment, there was a merging of the two neutrophil populations and the two T cell populations (**Fig. 4d, S9**). With expression level analysis, it was

observed that the rPS T cell population was predominately CD8+ (**Fig. S9b-d**). The single neutrophil population had low to neutral CD11b expression; there was no CD11b^{Hi} neutrophil population. In addition, with rPS treatment the monocyte population was expanded significantly, the DC population showed an upward trend in size (**Fig. 4d, S9a**). Furthermore, the rPS population produced a DC population with strong CD8 expression (**Fig. S9e**).

rPS treatment upregulates MHC II and induces costimulation blockade

To further understand the changes in immune cell populations as a result of rPS treatment, the inflammatory state of APC populations was assessed via receptor expression. Specifically, CD40, CD80 and CD86 coreceptor presentation on B cells, DCs and monocytes was analyzed (**Fig 5a, S10-13**). Furthermore, MHC II presentation (MHC II+ versus MHC II- blue) was assessed on DCs and monocytes (**Fig 5b, S10-13**). All analysis was conducted on blood, liver, draining axial and brachial and non-draining inguinal lymph nodes, and spleen. Marker expression consistent with costimulation blockade was significantly enhanced with rPS treatment (**Fig. 5a, S10-13**)[2]. Most significantly, rPS treatment conferred the loss of CD40 and CD80 expression, which occurred most significantly on DCs and monocytes in the draining axial and brachial lymph nodes (**Fig. 5ai,ii, S10-13**). In the draining lymph nodes, a significant decrease in coreceptor expression occurred for all APCs and receptor types except for CD86 expression on B cells (**Fig. 5a**). In blood, significant coreceptor downregulation of CD40 occurred in B cells, DCs and monocytes and of CD80 occurred in B cells and monocytes (**Fig. S10**). In the liver, only CD80 expression was significantly reduced with rPS treatment (**Fig. S11**). In the non-draining inguinal lymph nodes, CD40 and CD80 was significantly reduced on B cells, DCs and monocytes (**Fig. S12**). Monocytes and DCs of the spleen displayed significantly reduced CD80 expression following rPS treatment (**Fig. S13**). Regarding MHC II, rPS treatment significantly upregulated expression on both DCs and monocytes for all assessed tissues except for the liver (**Fig. 5b, S10-13**).

rPS treatment induces tolerogenic DCs and monocytes.

Further investigation into cell type-specific inflammatory makers and subpopulations was conducted for DCs and monocytes (**Fig. 6a**). For DCs, CD11c+ cells were subcategorized as conventional DCs type 1 (**cDC1s**; CD8+ CD11b-), conventional type 2 (**cDC2s**; CD8- CD11b+), conventional double positive (**DP** cDCs; CD8+

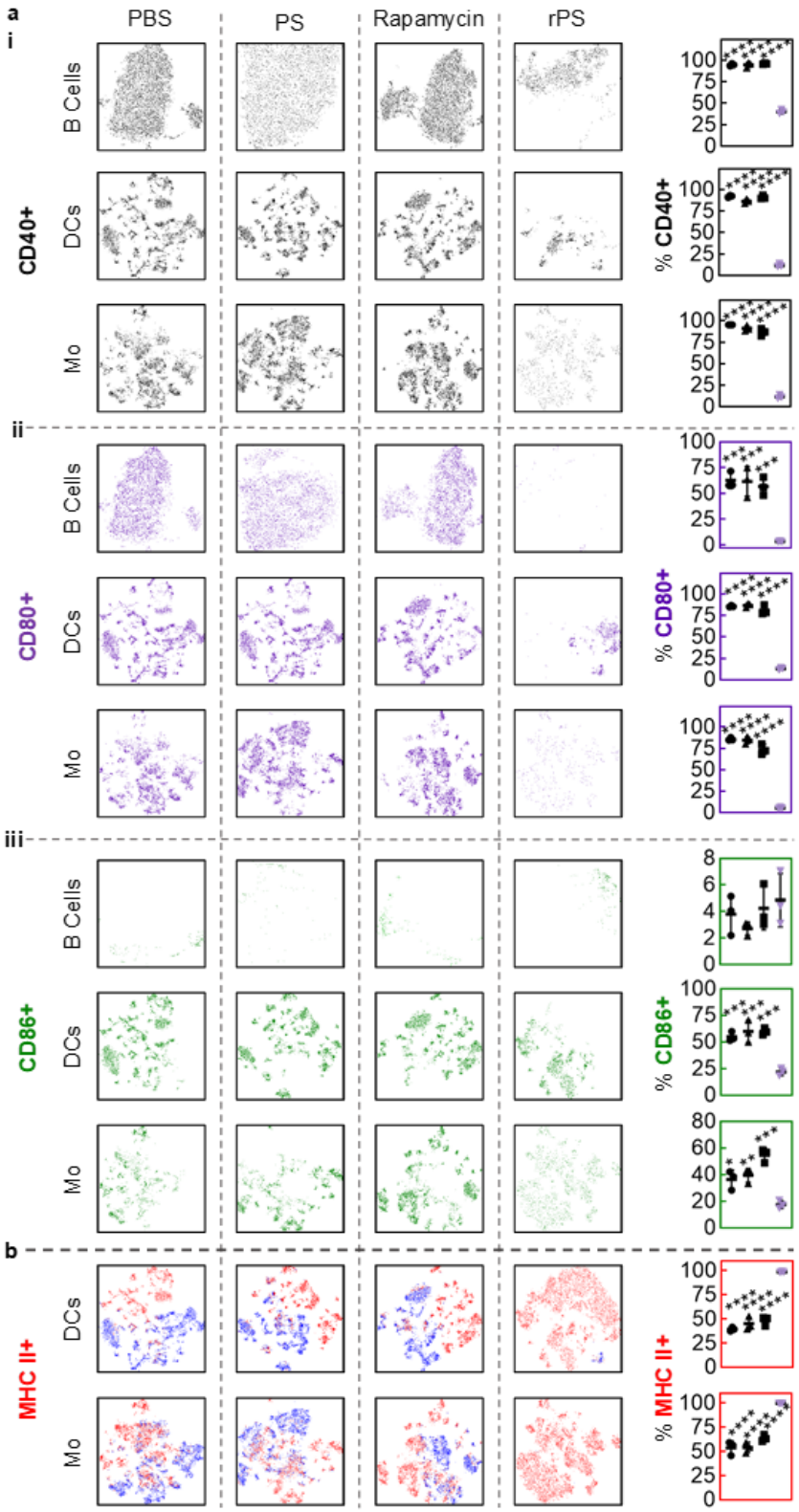

Fig. 5 | rPS altered immune cell populations induce costimulation blockade and upregulate MHC II. Mice were injected subcutaneously with (●), PS (▲), rapamycin (■) or rPS (▼) using the standard dosage protocol (11 injections, 1 mg/kg rapamycin or equivalent). Cell populations were analyzed by flow cytometry. (n = 3 mice). tSNE visualization of specific sub-CD45+ cells populations was performed. **a**, tSNE visualization of coreceptors CD40 (**a i**; black), CD80 (**a ii**; purple) and CD86 (**a iii**; forest green) on B cells, DCs and monocytes (Mo). **b,** tSNE visualization of MHC II presentation (MHC II+ red; MHC II- blue) on DCs and monocytes. All data presented above are for the draining axial and brachial lymph nodes. Analysis of blood, liver, non-draining inguinal lymph nodes and spleen is presented in **Fig. S10-13**, respectively. All data are presented as mean percentage (of B cells, DCs or monocytes) ± SD with *p<0.05; ** p<0.01; *** p<0.001; **** p<0.0001 relative to rPS treatment. Statistical significance was determined by one-way ANOVA with Tukey's multiple comparisons test.

CD11b+) or plasmacytoid DCs (**pDCs**) (**Fig. 6a**). Throughout all assessed tissues there was a trend of a reduced pDC population with rPS treatment (**Fig. 6a**). pDC downregulation was significant in the draining lymph nodes and spleen (**Fig. 6aiii,iv**). Interestingly, cDC1s significantly increased in the spleen (**Fig. 6aiv**). Furthermore, with the exception of the liver, rPS treatment induced an increase in CD8+ CD11b+ cDCs with significance in the draining lymph nodes (**Fig. 6ai,iii,iv**).

Regarding cells of the CD11b+ monocyte lineage, assessment of Ly-6C expression (Ly-6C^{Hi} versus Ly-6C^{Lo}) and macrophage markers (F4/80+ and/or CD169+ versus F4/80- and CD169-) was conducted. A significant reduction in Ly-6C expression was seen for all tissues with rPS treatment (**Fig. 6b, S16a**). Interestingly, while macrophages were significantly reduced with rPS treatment in the draining and non-draining lymph nodes (**Fig. 6biii, S16b**), the macrophage population was bolstered in the spleen and liver (**Fig. 6bii,iv**). It should be noted that while monocytes from the other treatment groups had a diverse mixture of monocyte and macrophage phenotypes, a single CD40- CD80- CD86- MHC II+ Ly-6C^{Lo} F4/80- CD169- phenotype dominated with rPS treatment, especially in lymph nodes (**Fig. 5, 6biii, S14**).

rPS induced, tolerogenic APCs modulate T cell populations.

Next, assessment of the T cell populations was conducted in order to determine the relationship between the inflammatory status of APCs and T cells in response to rPS treatment. In the blood, we observed several distinct populations of T cells including CD4+ CD8-, CD4- CD8+, DP CD4+ CD8+, double negative (**DN**) CD4- CD8-, NK, and CD4+ Tregs (**Fig. 7a**). Generally, the DP and CD4+ CD8- T cells tended to cluster together (**Fig. 7a**) as a result of the common level of expression of CD4 (**Fig. S17b,c**). The DP T cells had a relatively higher level of expression of CD4 as compared to CD8 (**Fig. S17b,c,d**). In contracts, the DN and CD4- CD8+ populations had their own distinct clusters (**Fig. 7a**). However, with rPS treatment, expression of both CD4 and CD8 were reduced (**Fig. S17b,c,d**). Furthermore, rPS treatment reduced the size of the CD4+ Treg population significantly, while the NK T cell population was significantly increased (**Fig. 7a, S17a**).

In the liver, generally, the single CD4- CD8+ T cell population dominated with CD8+ Tregs intermixed (**Fig. 7b, S18a**). On the periphery, smaller dispersed populations of DN and NK T cells were observed (**Fig. 7b**). However,

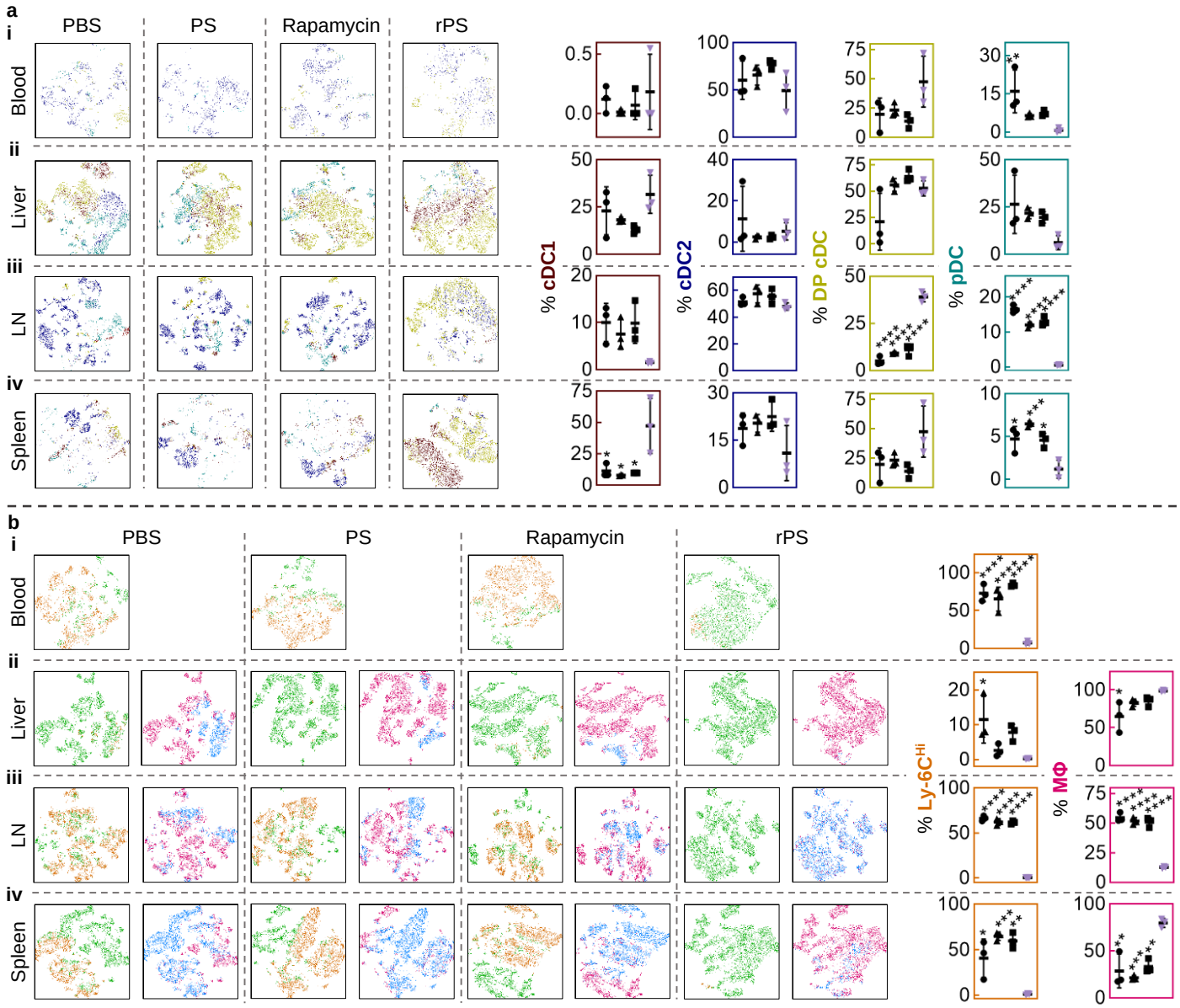

Fig. 6 | rPS treatment induces tolerogenic DCs and monocytes. Mice were injected subcutaneously with (●), PS (▲), rapamycin (■) or rPS (▼) using the standard dosage protocol (11 injections, 1 mg/kg rapamycin or equivalent). Cell populations were analyzed by flow cytometry. (n = 3 mice). tSNE visualization of specific sub-CD45+ cells populations was performed on blood (**i**), liver (**ii**), draining axial and brachial lymph nodes (**iii**), non-draining inguinal lymph nodes (**Fig. S15,16**) and spleen (**iv**). **a**, tSNE visualization of DC populations, including conventional DCs type 1 (cDC1; CD8+ CD11b-; maroon), conventional DCs type 2 (cDC2; CD8- CD11b+; navy), double positive conventional DCs (CD8+ CD11b+; citrus yellow), plasmacytoid dendritic cells (pDCs; teal). **b,** tSNE visualization of CD11b+ monocyte populations for expression of Ly-6C (Ly-6C^{Hi} mango orange; Ly-6C^{Lo} green) (left) and macrophage (MΦ) markers F4/80 and CD169 (F4/80+ and/or CD169+ rose; F4/80- and CD169- azure blue) (right). All data are presented as mean percentage (of DCs or monocytes) ± SD with *p<0.05; ** p<0.01; **** p<0.0001 relative to rPS treatment. Statistical significance was determined by one-way ANOVA with Tukey's multiple comparisons test.

with rPS treatment a significantly larger NK T cell population emerged while the CD8+ T cell populations declined (**Fig. 7b, S18a**). The DN T cell population was also enhanced with rPS treatment (**Fig. 7b, S18a**).

In the draining axial and brachial lymph nodes, the most distinct T cell clustering was observed. Highly defined CD4+ CD8-, CD4- CD8+, CD4+ Treg and DN T cell clusters were observed (**Fig. 7c**). While NK T cells were visible, no clear clustering pattern could be discerned (**Fig. 7c**). However, with rPS treatment, the CD4+ CD8- T

cell population was significantly reduced, as was CD4 expression within this population (**Fig. 7c, S19a,b,c**). A DP T cell population significantly emerged

and intermixed with the reduced CD4+ CD8+ T cell population (**Fig. 7c, S19a**). Furthermore, rPS treatment caused the DN T cell population to be significantly reduced (**Fig. 7c, S19a**). NK T cells were significantly enhanced and reside within the significantly expanded CD4- CD8+ T cell cluster (**Fig. 7c, S19a**), thus revealing their true nature as CD8+ NK T cells. Uniquely, the CD4+ Treg population was significantly reduced while the CD8+ Treg population was significantly enhanced (**Fig. 7c, S19a**). Similar effects were observed for the non-draining inguinal lymph nodes (**Fig. S20**).

Similar to the draining lymph nodes, splenic T cells primarily consisted of CD4+ CD8-, CD4- CD8+, CD4+ Treg and DN T cell clusters (**Fig. 7d**). Once more, NK T cells were observed, but without defined clustering (**Fig. 7d**). With rPS treatment, CD4- CD8+ T cells significantly increased (**Fig. 7d, S21a**). The CD4+ CD8- T cell population and CD4 expression within this population was significantly reduced and replaced by a significantly bolstered DP T cell population (**Fig. 7d, S21**). Furthermore, the CD4+ Treg population was significantly reduced (**Fig. 7d, S21a**).

Subcutaneous rapamycin delivery to APCs via rPS maintained normoglycemia at reduced rapamycin dosage after fully-MHC mismatched intraportal islet transplantation

In vivo assessment of rapamycin redistribution via rPS was conducted using a clinically relevant intraportal (liver) fully-MHC mismatched allogeneic islet transplantation model. Diabetes was induced in C57BL/6J mice via streptozotocin injection. To ensure the most stringent and severe model of T1D, diabetes was defined by blood glucose over 400 mg/dl[29]. A standard dosage protocol known to allow for fully-MHC mismatched allogeneic islet graft viability for more than 100 days was compared to a low dosage protocol (**Fig. 8a**). The standard dosage protocol consisted of 11 injections given daily. The low-dosage protocol consisted of 6 doses given every 3 days (**Fig. 8a**). All doses were equivalent (1 mg rapamycin per kg body weight) (**Fig. 8a**). Diabetic C57BL/6J mice received approximately 200 islets from fully MHC mismatched Balb/c mice in the liver via the portal vein (175 IEQ). Efficacy of the dosing regimen was confirmed by the restoration and maintenance of normoglycemia, confirming survival of the islet graft. As expected, mice that did not receive treatment all

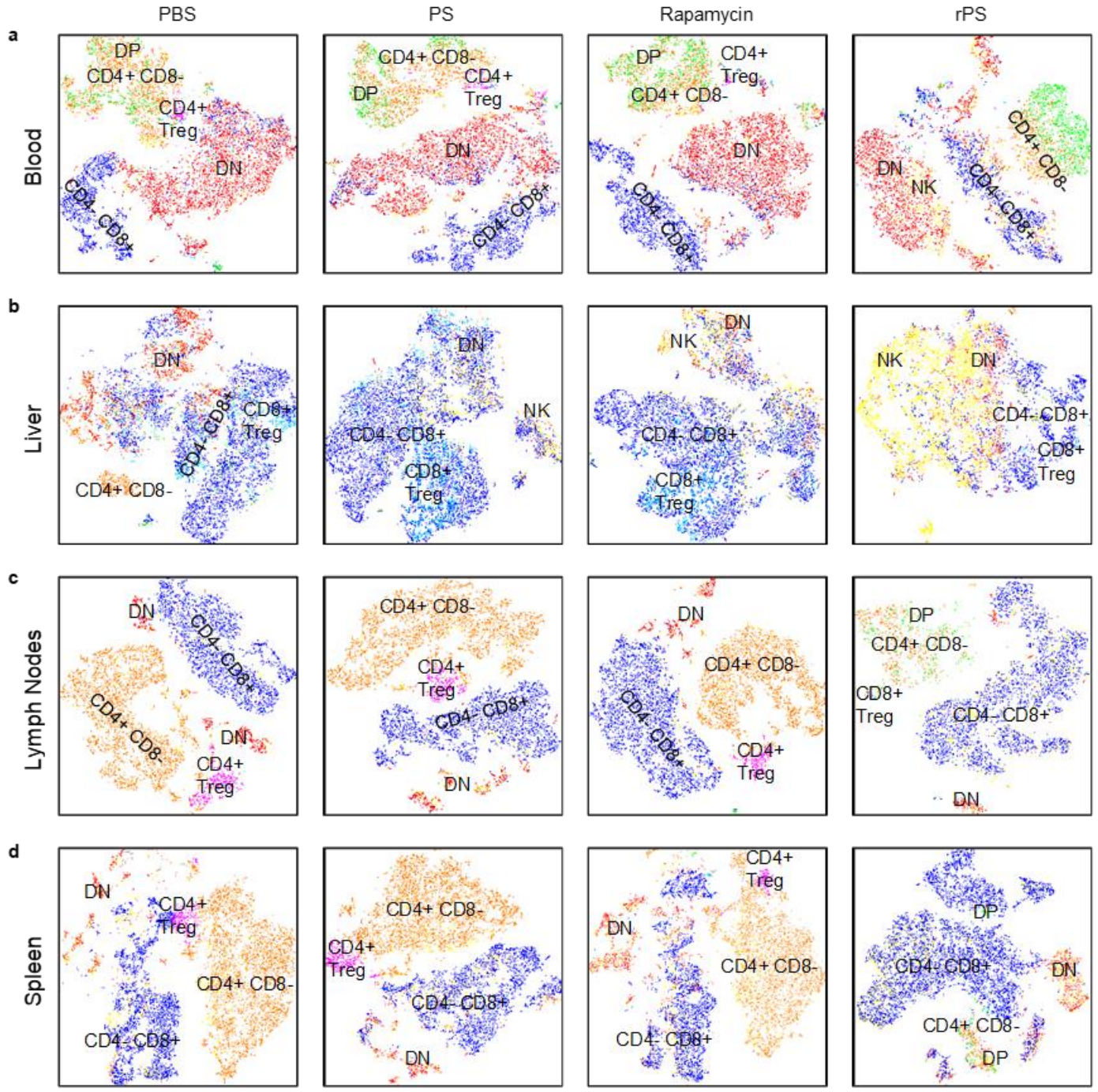

Fig. 7 | rPS induced, tolerogenic antigen-presenting cells modulate T cell populations. Mice were injected subcutaneously with PBS, PS, rapamycin or rPS using the standard dosage protocol (11 injections, 1 mg/kg rapamycin or equivalent). Cell populations were analyzed by flow cytometry. (n = 3 mice). tSNE visualization of specific sub-CD45+ cells populations as performed. **a**, tSNE visualization of CD3+ T cell populations, including CD4+ CD8- (orange), CD4- CD8+ (blue), DP CD4+ CD8+ (green), DN CD4- CD8- (red), CD4+ Treg (magenta), CD8+ Treg (light blue) and NK (yellow).

experienced graft rejection within 10 days of transplantation (**Fig. 8c,d**) and 71% of mice treated with the standard rapamycin protocol remained normoglycemic 100 days post transplantation (**Fig. 8c,d**). When the low-dosage protocol was used, only 33% of the mice treated with rapamycin remained normoglycemic 100 days post-transplantation, whereas 83% of (all, but one) mice treated with low-dosage rPS had normal blood glucose

concentrations (**Fig. 8c,d**). Furthermore, intraperitoneal glucose tolerance test (**IPGTT**), conducted at 30 days post-transplantation showed no difference in islet responsiveness with low dosage rPS treatment as compared to standard dosage rapamycin (**Fig. S22**).

Subcutaneous delivery of rapamycin to APCs via rPS avoids rapamycin side effects

We observed that mice treated with free rapamycin experienced injection site alopecia (**Fig. 8d**). Alopecia is a known side effect of rapamycin, impacting approximately 10% of patients[30]. While alopecia was reduced in the low dosage free rapamycin group (**Fig. 8d, S23**), no alopecia was observed in the low dosage rPS group (**Fig. 8e**). Histological analysis confirms our gross observations (**Fig. 8d**). Only immature follicles were identified in the standard rapamycin group (**Fig. 8d**) with some mature follicles present in the low dosage free rapamycin group (**Fig. 8d**). Organized mature follicles were identified in the low dosage rPS group (**Fig. 8d**). Furthermore, single cell RNA sequencing analysis of macrophages and CD4+ Tregs from the spleen and liver demonstrated that rPS mitigated expression of genes associated with rapamycin adverse effects. Specifically, rPS caused less inhibition of insulin-like growth factor 1 (**IGF1**), which is associated with impaired wound healing (**Fig. 8e, Table S1-2**). Oncogenes CRKL (V-Crk Avian Aarcoma Virus CT10) was downregulated with rPS treatment, whereas it was upregulated with rapamycin treatment[31] (**Fig. 8e, Table S1-2**). Tumor suppressor genes known to be downregulated by rapamycin, including MGAT1 (Mannosyl Glycoprotein Acetylglucosaminyl-Transferase 1)[32], PIK3R1 (Phosphoinositide-3-Kinase Regulatory Subunit 1)[33,34], PPP6R2 (Protein Phosphatase 6 Regulatory Subunit 2)[35], and ZDHHC3 (Zinc Finger DHHC-Type Palmitoyltransferase 3)[36] were less inhibited with rPS (**Fig. 8e, Table S1-2**). Furthermore, inhibition of genes associated with the regulation of metabolic processes caused by rapamycin, including ACAA1 (Acetyl-CoA Acyltransferase 1)[37] and PIK3R1[38], were reduced when rapamycin is given in rPS form (**Fig. 8e, Table S1-2**). Rapamycin causes downregulation of genes associated with the protective response to viral infection, including CD79A[39] and MZB1 (Marginal Zone B And B1 Cell Specific Protein)[40] (**Fig. 8e, Table S1-2**). The inhibition of these viral response genes was not seen with rPS treatment (**Fig. 8e, Table S1-2**).

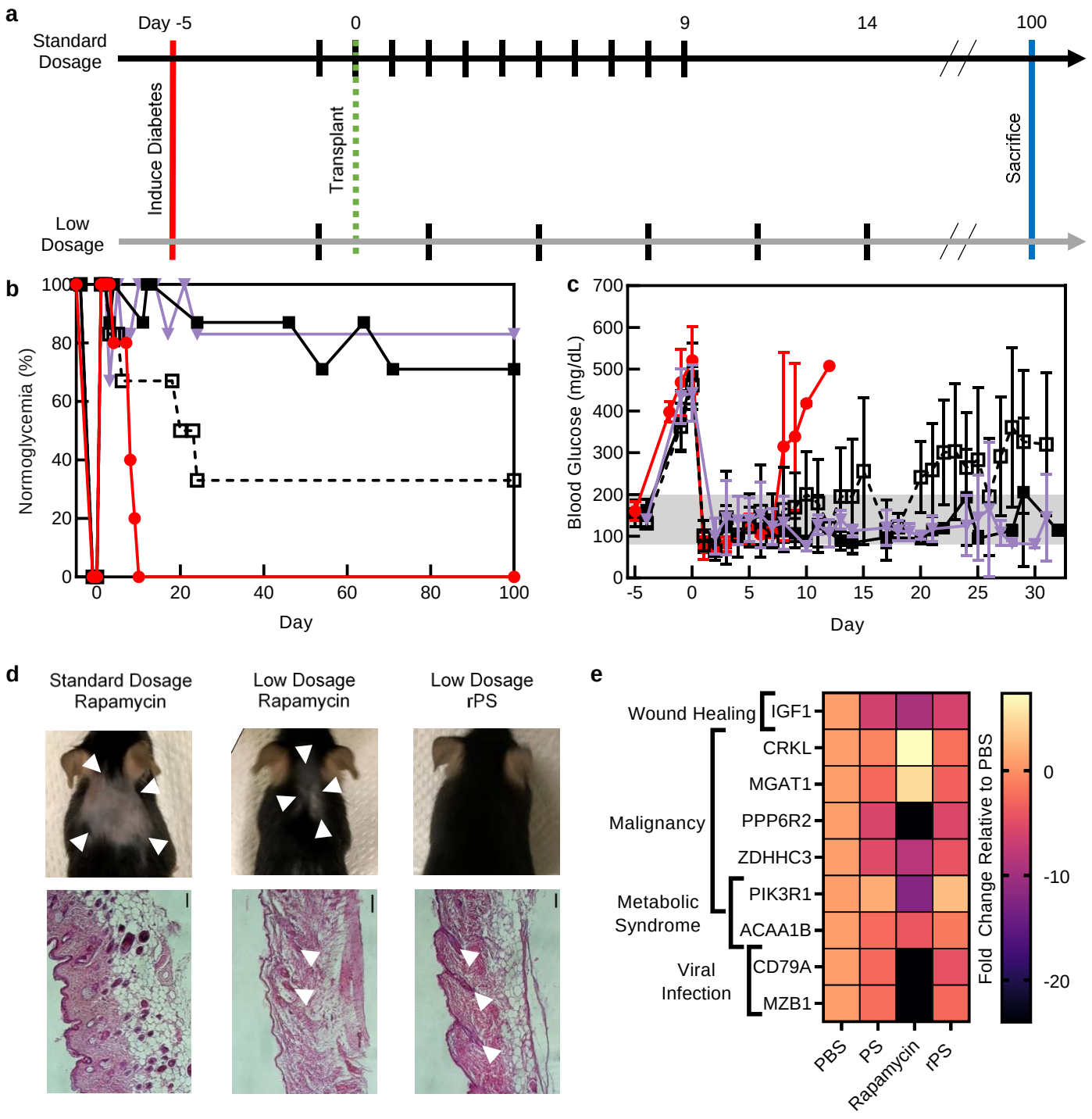

Fig. 8 | rPS reduce effective drug dose to achieve normoglycemia and mitigate side effects *in vivo*. a, Standard dosage and low dosage schemes for rapamycin during allogeneic islet transplantation (day 0) experiment. Diabetes is induced (day -5) via streptozotocin injection. The standard dosage protocol consists of 11 injections, given daily starting at day -1. The low dosage protocol consists of 6 injections, given every 3 days, starting at day -1. **b,** First month post-transplantation blood glucose concentrations. (n≥5 mice). **c,** Post-transplantation normoglycemia (%) (BG < 200 mg/dl). No treatment (—●—); Standard dosage rapamycin (—■—); Low dosage rapamycin (-⊟-); Low dosage rPS (—▼—). (n5-7 mice). **d,** Top: Digital photos of subcutaneous injection site on mouse dorsal showing alopecia 30 days after allogeneic islet transplantation by treatment group. Bottom: Hematoxylin and eosin histology of skin taking from mice 100 days post-transplantation with. White arrows show mature hair follicles. Scale bars represent 100 µm. (n 5-7 mice). **e,** Single cell RNA sequencing analysis of macrophages and Tregs from the liver and spleen of genes associated with known side effects of rapamycin, including impaired wound healing, malignancy, metabolic syndrome, and enhanced predisposition to viral infection. (n=3 mice). All data are presented as mean ± SD.

Discussion

A grand challenge of the pharmaceutical and biotechnology industries is to rationally engineer nanoscale drug carriers (i.e. nanocarriers) to selectively enhance modification of target cells while minimizing uptake by cells and organs responsible for side effects[41]. By controlling delivery kinetics and/or specificity to select cells and organs, nanocarriers can thus significantly change the therapeutic window of a drug and reduce undesired adverse events resulting from treatment[42]. Thus, nanocarriers can alter the interconnected network of cells contributing to observed therapeutic effects, which is particularly evident during immunotherapy when small subsets of immune cells can elicit potent cytokine and T cell responses. With these concepts in mind, we sought to investigate how subcutaneous delivery and nanocarrier-directed changes in the cellular biodistribution of rapamycin, a common therapeutic that elicits diverse cell-specific effects, could repurpose its mechanism of action at the cellular level to decrease side effects and enhance efficacy.

First off, the targeted cell population and the concentration of drug reaching this population needs to be considered. Rapamycin achieves immunosuppression by acting on T cells[43]. However, when given clinically using standard methods, the drug reaches other off-target cells leading to less drug reaching T cells[6,10,11]. Lack of specificity cannot be overcome with increased dosage given that rapamycin is associated with dose-dependent toxicity[6,10,11,43]. We have previously shown that giving drugs, including rapamycin, via PS, allows for enhanced uptake by APCs and little delivery to T cells[18,23]. Shuttling the drug to APCs using nanocarrier delivery, not only alters cellular level biodistribution, but also alters the amount of drug at the targeted cell type. Route of administration is another tool that is employed to impact biodistribution and overcome drug-specific barriers to delivery. Subcutaneous injection can overcome barriers associated with oral rapamycin such as diet-dependent bioavailability and variable metabolism via CYP3A4 and P-glycoprotein[43]. Using these tools—formulation and route of administration—the temporal, organ-level and cellular level biodistribution of a drug can be precisely manipulated for the desired effect. Herein, we show that subcutaneous delivery of rapamycin via PS creates a rapamycin biodistribution that perturbs the network of inflammatory cells in a manner that supports the survival of transplanted allogeneic islets. While others have attempted to use nanocarriers for altered delivery of rapamycin[10], to the best of our knowledge, we showcase the first attempt to deliver rapamycin via nanocarrier subcutaneously.

A drug's biodistribution is a blueprint mapping the inflammatory response at specific locations throughout an organism. Using subcutaneous injection, sustained delivery of a nanocarrier-loaded drug to the lymphatics can be achieved, as is observed with rapamycin delivery via PS (**Fig. 3a,b, S2**). Other tissues also benefit from sustained rapamycin concentration, including the blood, liver and spleen (**Fig. 3b, S3**). The enhanced rapamycin concentration in these tissues is attributed to the nature of the PS structure which is readily phagocytosed by APCs[23]. On the most fundamental level, a drug's biodistribution can influence the number of cells at a specific location. Given the sustained drainage to the lymph nodes observed with subcutaneous PS delivery, the most profound cellular effects are seen in this tissue (**Fig. 4c, S7a**). The most profound effects following rPS treatment include an upregulation of APCs and a down regulation of T cells (**Fig. 4**). Specifically, with rPS treatment, an increase in monocytes is observed in blood, draining and non-draining lymph nodes, and spleen (**Fig. 4a,c,d, S5a, S7a, S8a, S9a**). Furthermore, the DC population increases in both draining and non-draining lymph nodes and the spleen (**Fig. 4c,d, S7a, S8a, S9a**). Upregulation of NK cells is observed in blood and non-draining inguinal lymph nodes (**Fig. 4a, S5a, S8a**). Neutrophils show reduced expression of CD11b in blood, liver, and the spleen (**Fig. S5b,c, S6b,c, S9b,c**). CD11b downregulation is associated with an immature, anti-inflammatory state[44]. T cells are significantly reduced in the liver, draining and non-draining lymph nodes (**Fig. 4b,c, S6a, S7a, S8a**). These rPS induced cellular level modulations provide a foundation for an inflammatory environment that is amenable to allogenic islet transplantation. Upregulation of APCs has the potential to allow for enhanced uptake of the rPS particles. APCs have the ability to communicate with T cells to dictate inflammatory response[2,45]. Herein, we show a downregulation of T cells in immunomodulatory organs and at the site of intraportal islet transplantation—the liver (**Fig. 4b,c, S6a, S7a, S8a**). Given that the goal of immunosuppressive rapamycin therapy is to arrest the proliferation of T cells[43], an enhancement of this effect when this drug is given to APCs via PS is a sign of success. Thus, redistribution of our cellular network via rPS treatment establishes a foundation for cellular immunomodulation.

The secondary level of the biodistribution blueprint provides detail as to the inflammatory status of the modified cell populations. The rPS blueprint leverages the ability of APCs to communicate with T cells to induce an anti-inflammatory response. Specially, for islet transplantation, while direct donor antigen recognition by both CD4+ or CD8+ T cells and indirect presentation of donor antigen to CD8+ T cells contribute to a rejection

response, only indirect donor antigen presentation to CD4+ T cells is required for rejection[46]. The rPS biodistribution dictated blueprint of the inflammatory response is suitable for this application as CD4+ T cells are downregulated while CD8+ T cells are tolerized (**Fig. 7**). Therefore, we are able to take advantage of the following mechanisms in order to confer T cell tolerance: 1) costimulation blockade (**Fig. 5a**), 2) enhanced MHC II presentation (**Fig. 5b**), and 3) DC (**Fig. 6a**) and monocyte (**Fig. 6b**) populations with T cell tolerizing properties. Assessment of B cells, monocytes and DCs revealed widespread downregulation of coreceptors with rPS treatment (**Fig. 5a, S10-13**). Furthermore, monocytes and DCs have high expression of MHC II (**Fig. 5b, S10-13**). In order to induce an immune response, an MHC-T cell receptor (**TCR**) binding must occur between an APC and a T cells, in addition to coreceptor binding[2]. MHC II presentation on APCs is used to signal CD4+ TCRs[2]. As a result of rPS treatment, the high expression levels of MHC II on monocytes and DCs provides CD4+ T cells with MHC-TCR signaling for activation. However, the lack of costimulatory molecules on these APCs fails to provide CD4+ T cells with co-receptor stimulation. As a result, the CD4+ T cells go into a state of anergy and eventually undergo apoptosis[2]; thus, with rPS treatment, we observe a reduced CD4+ T cell population in all assessed tissues with the exception of the liver which has a minimal CD4+ T cell population generally (**Fig. 7, S5b,d,e, S6b,d,e, S7 b,d,e, S8 b,d,e, S9 b,d,e, S17, S19-21**).

In the lymph nodes and spleen, a significant upregulation of niche DP CD8+ CD11b+ cDCs are observed. Conventionally, it is understood that CD11b+ DCs cross-present to CD4+ T cells and CD8+ DCs cross-present to CD8+ T cells for induction of tolerance[47]. We hypothesize that for transplantation applications, this rare CD8+ CD11b+ DC population may have enhanced ability to phagocytose apoptotic donor cells and cross-present to both CD4+ and CD8+ T cells to induce tolerance[47]. Mature MHC II+ Ly-6C^{Lo} monocytes are a type of patrolling cell that is able to penetrate tissue during steady state conditions. Ly-6C^{Lo} monocytes have the ability to phagocytose both nanoparticles and apoptotic debris[25]. This non-classical monocyte population has a dual-fold advantage for transplantation applications, in which it supports an anti-inflammatory phenotype amenable to graft tolerance[48] and it has been shown to aid in the prevention of viral infections[49]. Mediated by programed death ligand 1 (PDL-1), these monocytes have the ability to cross present the apoptotic debris to CD8+ T cells and tolerize the CD8+ T cell, suppressing antigen specific responses[25]. Immunomodulation via PDL-1 has been

shown to enhance transplanted islet graft survival[50]. Thus, despite the large CD8+ T cell population observed in multiple tissues with rPS treatment (**Fig. 7, S17-21**), islet grafts remain viable (**Fig. 8b,c**).

The tolerogenic effects of rPS-treated APCs span beyond CD4+ and CD8+ T cells to create a hospitable environment of the islet graft. Niche T cell populations also make an important contribution to the congenial environment observed with rPS immunomodulatory therapy. The upregulation of DP CD4+ CD8+ T cells in the draining and non-draining lymph nodes and spleen (**Fig. 7c,d, S19-21**) has a dual function. DP T cells show suppressive functions, such as secreting anti-inflammatory cytokines under normal conditions, but enhanced responsiveness during infection, for example activating effector cells in the case of human immunodeficiency virus[51]. Furthermore, the CD8+ CD25+ FoxP3+ Tregs in the lymph nodes (**Fig. 7d, S19,20**) have enhanced suppressor capabilities relative to their CD4+ counterparts[52]. The tolerogenic properties of CD8+ Tregs are thought to prevent graft-versus-host disease and autoimmune diseases[52]. Despite their tolerized state, CD8+ T cells confer immunoprotection against pathogens[53]. This protective effect is augmented by the upregulation CD8+ NK T cells in all assess tissues (**Fig. 7, S17-21**), which have been shown to have enhanced ability to kill antigen-bearing DCs[54]; thus promoting tolerance.

Using formulation and route of administration as tools to modulate biodistribution, we establish an inflammatory network that is amenable to allogeneic islet transplantation without severe immune compromise. We present a clinically translatable model of islet transplantation for immunomodulatory therapy assessment. The use of the liver transplantation site is critical for translation of murine studies as the commonly used kidney capsule is not a feasible site for human islet transplantation[29]. Kidney capsule transplantation fails to expose the islets to the immune environment of the liver[29]. For example, islets transplanted to the kidney capsule are not exposed to blood to induce the instant blood-mediate inflammatory reaction (IBMIR)[29]. Additionally, the exposure of the islets to immunosuppressive drugs differs between the liver and kidney capsule transplantation site[29]. Furthermore, MHC molecules are the most significant allo-antigens involved in graft rejection, thus using a fully MHC-mismatched model is critical for rigorous assessment of allogeneic transplantation. Furthermore, it is important to note that all combinations of fully mismatched mouse models confer the same potency and kinetics of allo-immune response. We utilized the combination of Balb/c islets transplanted into C57BL/6J recipient mice, which provides the greatest challenge to islet survival and normoglycemia restoration[29]. Utilizing excess islets

can delay the graft rejection, giving a false sense of maintained normoglycemia and immunosuppression. While other models use up to 1000 islet equivalents (**IEQ**)[55,56], our model uses a minimal islet mass of only ~200 murine islets (~175 IEQ). The translatability of the model is enhanced by the subcutaneous route administration, which fosters lymphatic drainage (**Fig. 3a,b**). Furthermore, this route of administration overcomes some of the challenges that have historically plagued the oral, nanocrystal formulation of rapamycin, Rapamune®[6]. Specifically, subcutaneous delivery of rapamycin improves bioavailability over oral delivery as first pass metabolism and p-glycoprotein efflux are avoided[9,10]. Variability of bioavailability as food intake is not an influencing factor for subcutaneous injection. Many murine studies involving rapamycin use intraperitoneal injection, however this route is not easily translatable to humans. Finally, subcutaneous injection is advantageous over intravenous infusion as patients can perform the injection in their own home, as opposed to having to visit their doctor. In summary, this work lays a foundation for a novel method of repurposing clinically used drugs by targeting them to alternative cell populations for enhanced efficacy and mitigated adverse effects.

Materials and Methods

Animals

8 to 12-week-old, male C57BL/6J and Balb/c mice were purchased from Jackson Labs. Mice were housed in the Center for Comparative Medicine at Northwestern University. All animal protocols were approved by Northwestern University's Institutional Animal Care and Use Committee (IACUC).

Materials

Unless explicitly stated below, all reagents and chemicals were purchased from Sigma-Aldrich.

Polymer Synthesis

Poly(ethylene glycol)-*block*-poly(propylene sulfide) (PEG-*b*-PPS) was synthesized as previously described by us[18]. In brief, methyl ether PEG (MW 750) was functionalized with mesylate. The mesylate was reacted with thioacetic acid to form PEG-thioacetate and then base activating the thioacetate to form a thiolate anion and initiate ring opening polymerization of propylene sulfide. Benzyl bromide was used as an end-capping agent to

form PEG_{17}-*b*-PPS_{30}-Bz or the thiolate anion was protonated to form PEG_{17}-*b*-PPS_{30}-SH. The polymer was characterized by H-NMR and gel permeation chromatography (GPC).

Nanocarrier Formulation

PS were formed via thin film hydration, as previously described[18,57]. In brief, 20 mg of PEG_{17}-*b*-PPS_{30}-Bz was weighted in a sterilized 1.8 ml glass HPLC vial. 750 ul of dichloromethane (DCM) was added to the vial. To form, rPS 0.5 mg of rapamycin, dissolved at 25 mg/ml in ethanol, was also added. The vial was desiccated to remove the DCM. Next, 1 ml of phosphate-buffered saline (PBS) was added to the vial. The vials were shaken at 1500 rpm overnight. PS were extruded multiple times first via 0.2 um and then 0.1 um syringe filters. Excess rapamycin was removed via size exclusion chromatography using a Sephadex LH-20 column with 1XPBS.

Nanocarrier Characterization

DLS: DLS measurements were performed on a Nano 300 ZS Zetasizer (Malvern) and were used to determine nanocarrier diameter distribution and corresponding polydispersity index.

cryoTEM: 200-mesh lacey carbon grids were glow-discharged for 30 seconds in a Pelco easiGlow glow-discarger at 15mA with a chamber pressure of 0.24 mBar. 4 µL of sample was then pipetted onto the grid and plunge-frozen into liquid ethane in a FEI Vitrobot Mark III cryo plunge freezing device for 5 seconds with a blot offset of 0.5mm. Grids were then loaded into a Gatan 626.5 cryo transfer holder, imaged at –172 °C in a JEOL JEM1230 LaB6 emission TEM at 100kV, and the data was collected on a Gatan Orius 2k x 2k camera.

SAXS: SAXS was performed at Argonne National Laboratory's Advanced Photo Source with collimated X-rays (10 keV; 1.24 Å). Data reduction was performed using Primus software and modeling was performed using SASView.

Quantification of Rapamycin Loading[18]

rPS nanocarriers (50 ul) were lyophilized and re-dissolved in HPLC grade DMF. Salts were removed via centrifugation at 17,000 g for 10 minutes. Rapamycin content of the nanocarriers was characterized via HPLC (Thermo Fisher Dionex UltiMate 3000) using an Agilent Polypore 7.5 x 300 mm column and an Agilent Polypore

7.5 x 50 mm guard column. The system was housed at 60°C. DMF (0.5 ml/minute) was used as the mobile phase. Rapamycin was detected at 270 nm. Thermo Scientific Chromeleon software was used for analysis. The concentration of rapamycin was characterized via the area under the curve in comparison to a standard curve of rapamycin concentrations.

Rapamycin Stability in Nanocarrier

rPS formulations were fabricated as previously described. Formulations were stored at 4°C in glass scintillation vials. At various time points, the formulations were vortexed, 1 ml samples were transferred to Millipore Amicon Ultra Centrifuge 10,000 NMWL Tubes and centrifuged at 4000 g in a swinging bucket rotor to remove unloaded drug. The retentate was brought back up to its original volume using 1XPBS. Quantification of rapamycin was performed as previously described.

Immunomodulation Study

Healthy C57BL/6J mice were subjected to a “standard dosage regime.” Animals were injected subcutaneously for 11 days with rapamycin (in 0.2% CMC) or rPS at a dose of 1 mg/kg. Equivalent dose of 1XPBS or PS were injected as controls. After 11 days, the mice were sacrificed. Blood, lymph nodes (axial, brachial, and inguinal), liver and spleen were collected and processed for flow cytometry.

Flow cytometry

Blood was spun down at 3000 g for 25 minutes to separate the plasma and blood cells. The blood cells were treated with 1X red blood cell lysis buffer (Fisher) for 5 minutes on ice, washed with 1XPBS and spun down, thrice. The liver was minced, treated with collagenase for 45 minutes at 37 °C, processed through a 70 nm filter, and then treated with 1X red blood cell lysis buffer (Fisher) for 5 minutes on ice, washed with 1X PBS and spun down. The spleen was processed through a 70 nm filter and treated with 1X red blood cell lysis buffer (Fisher) for 5 minutes on ice, washed with 1XPBS and spun down. Lymph nodes were passed through a 70 nm filter, washed with 1XPBS and spun down. All cells were resuspended in a cocktail of Zombie Near Infrared (BioLegend) for viability and anti-mouse CD16/CD32 for FcR blocking with BD Brilliant Violet cell staining buffer

and incubated at 4 °C for 15 minutes. Next, an antibody cocktail consisting of Pacific Blue anti-mouse CD11c (BioLegend), BV480 anti-mouse NK1.1 (BD), BV510 anti-mouse CD19 (BioLegend), BV570 anti-mouse CD3 (BioLegend), BV650 anti-mouse F4/80 (BioLegend), BV650 anti-mouse MHC II (IA-IE) (BioLegend), BV711 anti-mouse Ly-6C (BioLegend), BV750 anti-mouse CD45R/B220 (BioLegend), BV785 anti-mouse CD11b (BioLegend), AF532 anti-mouse CD8a (Invitrogen), PerCP-Cy5.5 anti-mouse CD45 (BioLegend), PerCp-eFluor711 anti-mouse CD80 (Invitrogen), PE-Dazzle594 anti-mouse CD25 (BioLegend), PE-Cy5 anti-mouse CD4 (BioLegend), PE-Cy7 anti-mouse CD169 (BioLegend), APC anti-mouse FoxP3 (Invitrogen), AF647 anti-mouse CD40 (BioLegend), APC-R700 anti-mouse Ly-6G (BioLegend), and APC/Fire 750 anti-mouse CD86 (BioLegend) was added to the cells and incubated for 20 minutes at 4 °C. The cells were washed with 1X PBS, fixed and permeabilized using a FoxP3 Fix/Perm Kit (BioLegend), according to the manufacturer's protocol. Next, anti-mouse FoxP3 was added and incubated for 30 minutes in the dark at room temperature. Finally, cells were washed twice with 1XPBS and resuspended in cell buffer. The cells were analyzed on an Aurora flow cytometer (CyTek). Spectral unmixing was performed using SpectroFlo (CyTek) and analysis was performed using FloJo software. Gating was performed as outlined in Fig. S59[58,59].

tSNE

For each analysis, FlowJo's DownSample plugin was used to randomly select an equal number of events from each cell population (CD45+, CD45+ CD3+, CD45+ CD19+, CD45+ CD11b+, or CD45+ CD11c+) of every sample. The purpose of DownSample was to both normalize the contribution of each mouse replicate and reduce computational burden. Next, samples from mice that underwent the same treatment and same cell population were concatenated. The tSNE plugin was run on concatenated samples using the Auto opt-SNE learning configuration with 3000 iterations, a perplexity of 50 and a learning rate equivalent to 7% of the number of events[60]. The KNN algorithm was set to exact (vantage point tree) and the Barnes-Hut gradient algorithm was employed.

Indocyanine Green Biodistribution

Indocyanine green (ICG) PS were formed using thin film rehydration, as previously described[57]. In brief, 20 mg of PEG_{17}-*b*-PPS_{30}-Bz was weighted in a sterilized 1.8 ml glass HPLC vial. 750 ul of dichloromethane (DCM) was added to the vial. The vial was desiccated to remove the DCM. Next, 1 ml of 0.258 mM ICG in 1XPBS was added to the vial. The vials were shaken at 1500 rpm overnight. PS were extruded multiple times first via 0.2 um and then 0.1 um syringe filters. Float-A Lyzer G2 Dialysis devices (Fisher) were used to remove unloaded ICG. ICG loading was quantified relative to standards composed of known amounts of polymer and ICG in a 1:33 molar ratio using absorbance at 820 nm as previously described by our group[57]. C57BL/6J mice received subcutaneous injections of either free ICG (in 1XPBS) or ICG-PS. ICG concentration was matched at 50 ug/ml. The injection volume was 150 ul. At 2, 24- and 48-h post-injection, the mice were sacrificed, blood was collected via cardiac puncture, and perfusion was performed using heparinized 1XPBS. Liver, spleen, kidneys, heart and lung were harvested and imaged via IVIS Lumina with an excitation wavelength of 745 nm, an emission wavelength of 810 nm, an exposure time of 2 seconds and a f/stop of 2.

Rapamycin Biodistribution

Mice were injected with rapamycin (in 0.2% CMC) or rPS at 1 mg/ml and sacrificed at the following time points: 0.5, 2, 8, 16, 24, and 48 h. Urine was collected via metabolic cages during the duration between injection and sacrifice for the 8, 16, 24 and 48-h timepoints. The following tissues and/or organs were collected: blood, spleen, liver, kidneys, heart, brain, lungs, lymph nodes (axial and brachial), and fat pad. Rapamycin was extracted from blood and urine using a solution of methanol and acetonitrile (50:50 v/v) doped with rapamycin-D3 (Cambridge Isotope Laboratories) as an internal standard. Tissue samples were homogenized in homogenization tubes prefilled with stainless steel ball bearings (Sigma) using a solution of phosphoric acid (8%), acetonitrile and acetic acid (30:67.2:2.8 v/v/v). After homogenization, tissue samples were also doped with rapamycin-D3. All samples were precipitated via incubation at -20 °C, followed by centrifugation. The supernatant was collected and LC-MS/MS (Shimadzu LC-30AD pumps; SIL-30ACMP autosampler; CBM-20A oven; Sciex Qtrap 6500) was used to determine rapamycin concentration. Rapamycin had a retention time of 2.7 minutes. Rapamycin-D3 had a retention time of 3.0 minutes.

Allogeneic Islet Transplantation

Diabetes was induced via streptozotocin (IP; 190 mg/kg) injection five days prior to transplantation and confirmed via hyperglycemia (blood glucose > 400 mg/dl). Starting the day prior to transplantation, mice were injected with PBS, PS, rapamycin, or rPS (N=3 per group) at 1 mg/kg (or equivalent) in accordance with a standard dosage (11 doses, given daily) or a low dosage (6 doses, given every 3rd day). On the day of transplantation, islets were isolated from Balb/c mice via common bile duct cannulation and pancreas distension with collagenase. Islets isolated from two donors (~200 mouse islets, ~175 IEQ) were transplanted to C57B6/J recipients via the portal vein. Body weight and blood glucose concentration were monitored closely for 100 days post-transplantation. Intraperitoneal glucose tolerance test (IPGTT) was performed one-month post transplantation. The animals were fasted for 16 h before being injected intraperitoneally with 2 g dextrose (200 g/L; Gibco) per kg body weight. Blood glucose concentrations were measured at 0, 15, 30, 60- and 120-minutes post-injection.

Alopecia Assessment

Dorsal photos were taken weekly to assess for alopecia. At 100-days post-transplantation, the mice were euthanized, and skin samples were excised in the dorsal region at the subcutaneous injection site. Skin samples were placed in cassettes, fixed in 4% paraformaldehyde, and embedded in paraffin. Tissue blocks were sectioned at a thickness of 5 nm and stained with hematoxylin and eosin (H&E). Digital images were taken on a Nikon microscope.

Single Cell RNA Sequencing

Healthy C57BL/6J mice were subjected to a “standard dosage regime.” Animals were injected subcutaneously for 11 days with rapamycin (in 0.2% CMC) or rPS at a dose of 1 mg/kg. Equivalent dose of 1XPBS or PS were injected as controls. After 11 days, the mice were sacrificed, and the liver and spleen were excised. The organs were processed as was done for flow cytometry. CD4+ Tregs and macrophages were isolated using magnetic sorting (MojoSort; BioLegend). Briefly, cells were first incubated in a cocktail of PE anti-mouse CD169 and PE anti-mouse F4/80 antibodies (BioLegend). After washing, incubation in anti-PE nanobeads (BioLegend) occurred. Macrophages were magnetically sorted from non-macrophages. The non-macrophages cell fraction

was then incubated in mouse CD4+ T cell isolation biotin-antiboy cocktail (BioLegend) and sorted. The CD4+ T cell fraction was then incubated in APC anti-mouse CD25 antibody (BioLegend), followed by washing, incubation in anti-APC nanobeads (BioLegend) and sorting. RNA was isolated from separated macrophages and CD4+ Tregs using RNeasy Mini Kit with DNAse digestion (Qiagen). Samples were frozen and shipped to Admera Health where they underwent library preparation using the Lexogen 3‘ mRNA-Seq Library Prep Kit FWD HT (Lexogen) and were sequenced on an Illumina sequencer (HiSeq 2500 2 x 150 bp). For each pair, Read 2 was discarded and only Read 1 was used for downstream data analysis. Sequencing quality was analyzed with FastQC v0.11.5[61] and reads were trimmed and filtered with Trimmomatic v0.39[62]**.** One sample from the spleen T cell PBS treatment group and one sample from the spleen T cell rapamycin treatment group were discarded due to low sequencing quality. Reads were aligned with STAR v2.6.0a [63] to the GRCm38.p6 mouse reference genome primary assembly using the GRCm38.p6 mouse reference primary comprehensive gene annotation (https://www.gencodegenes.org/mouse/). Quantification and differential expression was performed with Cuffdiff from Cufflinks v2.2.1[64-66] again using the GRCm38.p6 mouse reference primary comprehensive gene annotation and a 0.05 FDR. Detailed settings for each software are included in Table S1. The raw data displayed in Fig. 8e broken down by cell type is in Table S2.

Acknowledgements

Alex D. Jerez designed and created the illustration in Figure 1. Modifications were made by J.B.

This work made use of funding from the Center for Advanced Regenerative Engineering (CARE), the Flow Cytometry Facility at the University of Chicago, the Integrated Molecular Structure Education and Research Center (IMSERC) at Northwestern University, which has received support from the Soft and Hybrid Nanotechnology Experimental (SHyNE) Resource (NSF ECCS-1542205), the State of Illinois, and the International Institute for Nanotechnology (IIN), the Northwestern University Center for Advanced Molecular Imaging (CAMI), which is generously supported by NCI CCSG P30 CA060553 awarded to the Robert H Lurie Comprehensive Cancer Center; the BioCryo facility of Northwestern University’s NU*ANCE* Center, which has received support from the Soft and Hybrid Nanotechnology Experimental (SHyNE) Resource (NSF ECCS-1542205); the MRSEC program (NSF DMR-1720139) at the Materials Research Center; the International Institute for Nanotechnology (IIN); and the State of Illinois, through the IIN. It also made use of the CryoCluster

equipment, which has received support from the MRI program (NSF DMR-1229693). This research was supported by the National Science Foundation (CAREER Award no. 1453576) and the National Institutes of Health Director's New Innovator Award (NHLBI 1DP2HL132390-01).

Author Contributions

J.B. designed the experiments with the assistance of S.D.. J.B., X.Z., S.B., M.F., C.B., and H.H. performed the experiments. R.R. performed computational analysis on the RNA sequencing data with oversight from LA. JB analyzed the data and composed the manuscript. E.S. and G.A. supervised the study.

Competing Interests

J.B., S.D., E.S., and G.A. are coinventors on a patent application related to the work presented in this manuscript.

References

1 Atkinson, M. A., Eisenbarth, G. S. & Michels, A. W. Type 1 diabetes. *The Lancet* **383**, 69-82 (2014).

2 Abbas, A. K. & Lichtman, A. H. *Basic immunology : functions and disorders of the immune system*. 2nd edn, (Saunders, 2004).

3 Shapiro, A. M., Pokrywczynska, M. & Ricordi, C. Clinical pancreatic islet transplantation. *Nat Rev Endocrinol* **13**, 268-277, doi:10.1038/nrendo.2016.178 (2017).

4 Stock, P. G. & Bluestone, J. A. Beta-cell replacement for type I diabetes. *Annu Rev Med* **55**, 133-156, doi:10.1146/annurev.med.55.091902.103539 (2004).

5 Molano, R. D. *et al.* Long-term islet allograft survival in nonobese diabetic mice treated with tacrolimus, rapamycin, and anti-interleukin-2 antibody. *Transplantation* **75**, 1812-1819 (2003).

6 Berney, T. & Secchi, A. Rapamycin in islet transplantation: friend or foe? *Transpl Int* **22**, 153-161, doi:10.1111/j.1432-2277.2008.00743.x (2009).

7 Wiseman, A. C. Immunosuppressive Medications. *Clin J Am Soc Nephrol* **11**, 332-343, doi:10.2215/CJN.08570814 (2016).

8 Halloran, P. F. Immunosuppressive drugs for kidney transplantation. *N Engl J Med* **351**, 2715-2729, doi:10.1056/NEJMra033540 (2004).

9 Inc), W. P. L. P. Rapamune® (sirolimus). *U.S. Food and Drug Administration* (2020).

10 Haeri, A., Osouli, M., Bayat, F., Alavi, S. & Dadashzadeh, S. Nanomedicine approaches for sirolimus delivery: a review of pharmaceutical properties and preclinical studies. *Artif Cells Nanomed Biotechnol* **46**, 1-14, doi:10.1080/21691401.2017.1408123 (2018).

11 Yatscoff, R. W., Wang, P., Chan, K., Hicks, D. & Zimmerman, J. Rapamycin: distribution, pharmacokinetics, and therapeutic range investigations. *Ther Drug Monit* **17**, 666-671 (1995).

12 Napoli, K. L., Wang, M. E., Stepkowski, S. M. & Kahan, B. D. Distribution of sirolimus in rat tissue. *Clin Biochem* **30**, 135-142 (1997).

13 Ferron, G. M., Mishina, E. V., Zimmerman, J. J. & Jusko, W. J. Population pharmacokinetics of sirolimus in kidney transplant patients. *Clin Pharmacol Ther* **61**, 416-428, doi:10.1016/S0009-9236(97)90192-2 (1997).

14 Meier-Kriesche, H. U. & Kaplan, B. Toxicity and efficacy of sirolimus: relationship to whole-blood concentrations. *Clin Ther* **22 Suppl B**, B93-100 (2000).

15 Hafiz, M. M. *et al.* Immunosuppression and procedure-related complications in 26 patients with type 1 diabetes mellitus receiving allogeneic islet cell transplantation. *Transplantation* **80**, 1718-1728 (2005).

16 Stabler, C. L., Li, Y., Stewart, J. M. & Keselowsky, B. C. Engineering immunomodulatory biomaterials for type 1 diabetes. *Nature Reviews Materials* **4**, 429-450 (2019).

17 Simamora, P., Alvarez, J. M. & Yalkowsky, S. H. Solubilization of rapamycin. *Int J Pharm* **213**, 25-29, doi:10.1016/s0378-5173(00)00617-7 (2001).

18 Allen, S., Osorio, O., Liu, Y. G. & Scott, E. Facile assembly and loading of theranostic polymersomes via multi-impingement flash nanoprecipitation. *J Control Release* **262**, 91-103, doi:10.1016/j.jconrel.2017.07.026 (2017).

19 Allen SD, L. Y., Bobbala S, Cai L, Hecker PI, Temel R, Scott EA. Polymersomes scalably fabricated via flash nanoprecipitation are non-toxic in non-human primates and associate with leukocytes in the spleen and kidney following intravenous administration. *Nano Research*, doi:10.1007/s12274-018-2069-x (2018).

20 Stano, A., Scott, E. A., Dane, K. Y., Swartz, M. A. & Hubbell, J. A. Tunable T cell immunity towards a protein antigen using polymersomes vs. solid-core nanoparticles. *Biomaterials* **34**, 4339-4346, doi:10.1016/j.biomaterials.2013.02.024 (2013).

21 Scott, E. A. *et al.* Dendritic cell activation and T cell priming with adjuvant- and antigen-loaded oxidation-sensitive polymersomes. *Biomaterials* **33**, 6211-6219, doi:10.1016/j.biomaterials.2012.04.060 (2012).

22 Dowling, D. J. *et al.* Toll-like receptor 8 agonist nanoparticles mimic immunomodulating effects of the live BCG vaccine and enhance neonatal innate and adaptive immune responses. *J Allergy Clin Immunol* **140**, 1339-1350, doi:10.1016/j.jaci.2016.12.985 (2017).

23 Yi, S. *et al.* Tailoring Nanostructure Morphology for Enhanced Targeting of Dendritic Cells in Atherosclerosis. *ACS Nano* **10**, 11290-11303, doi:10.1021/acsnano.6b06451 (2016).

24 Bracho-Sanchez, E., Hassanzadeh, A., Brusko, M. A., Wallet, M. A. & Keselowsky, B. G. Dendritic Cells Treated with Exogenous Indoleamine 2,3-Dioxygenase Maintain an Immature Phenotype and Suppress Antigen-specific T cell Proliferation. *J Immunol Regen Med* **5**, doi:10.1016/j.regen.2019.100015 (2019).
25 Peng, Y., Latchman, Y. & Elkon, K. B. Ly6C(low) monocytes differentiate into dendritic cells and cross-tolerize T cells through PDL-1. *J Immunol* **182**, 2777-2785, doi:10.4049/jimmunol.0803172 (2009).
26 Getts, D. R. *et al.* Therapeutic inflammatory monocyte modulation using immune-modifying microparticles. *Sci Transl Med* **6**, 219ra217, doi:10.1126/scitranslmed.3007563 (2014).
27 Allen, R. P., Bolandparvaz, A., Ma, J. A., Manickam, V. A. & Lewis, J. S. Latent, Immunosuppressive Nature of Poly(lactic-co-glycolic acid) Microparticles. *ACS Biomater Sci Eng* **4**, 900-918, doi:10.1021/acsbiomaterials.7b00831 (2018).
28 Emoto, C., Fukuda, T., Cox, S., Christians, U. & Vinks, A. A. Development of a Physiologically-Based Pharmacokinetic Model for Sirolimus: Predicting Bioavailability Based on Intestinal CYP3A Content. *CPT Pharmacometrics Syst Pharmacol* **2**, e59, doi:10.1038/psp.2013.33 (2013).
29 Cantarelli, E. *et al.* Murine animal models for preclinical islet transplantation No model fits all (research purposes). *Islets* **5**, 79-86 (2013).
30 Mahe, E. *et al.* Cutaneous adverse events in renal transplant recipients receiving sirolimus-based therapy. *Transplantation* **79**, 476-482 (2005).
31 Song, Q. *et al.* CRKL regulates alternative splicing of cancer-related genes in cervical cancer samples and HeLa cell. *BMC Cancer* **19**, 499, doi:10.1186/s12885-019-5671-8 (2019).
32 Akiva, I. & Birgul Iyison, N. MGAT1 is a novel transcriptional target of Wnt/beta-catenin signaling pathway. *BMC Cancer* **18**, 60, doi:10.1186/s12885-017-3960-7 (2018).
33 Lin, Y. *et al.* PIK3R1 negatively regulates the epithelial-mesenchymal transition and stem-like phenotype of renal cancer cells through the AKT/GSK3beta/CTNNB1 signaling pathway. *Sci Rep* **5**, 8997, doi:10.1038/srep08997 (2015).
34 Vallejo-Diaz, J., Chagoyen, M., Olazabal-Moran, M., Gonzalez-Garcia, A. & Carrera, A. C. The Opposing Roles of PIK3R1/p85alpha and PIK3R2/p85beta in Cancer. *Trends Cancer* **5**, 233-244, doi:10.1016/j.trecan.2019.02.009 (2019).
35 Zhong, J. *et al.* Protein phosphatase PP6 is required for homology-directed repair of DNA double-strand breaks. *Cell Cycle* **10**, 1411-1419, doi:10.4161/cc.10.9.15479 (2011).
36 Kinney, N., Varghese, R. T., Anandakrishnan, R. & Garner, H. R. S. ZDHHC3 as a Risk and Mortality Marker for Breast Cancer in African American Women. *Cancer Inform* **16**, 1176935117746644, doi:10.1177/1176935117746644 (2017).
37 Cazanave, S. *et al.* The Transcriptomic Signature Of Disease Development And Progression Of Nonalcoholic Fatty Liver Disease. *Sci Rep* **7**, 17193, doi:10.1038/s41598-017-17370-6 (2017).
38 Thauvin-Robinet, C. *et al.* PIK3R1 mutations cause syndromic insulin resistance with lipoatrophy. *Am J Hum Genet* **93**, 141-149, doi:10.1016/j.ajhg.2013.05.019 (2013).
39 Havranek, O. *et al.* Tonic B-cell receptor signaling in diffuse large B-cell lymphoma. *Blood* **130**, 995-1006, doi:10.1182/blood-2016-10-747303 (2017).
40 Andreani, V. *et al.* Cochaperone Mzb1 is a key effector of Blimp1 in plasma cell differentiation and beta1-integrin function. *Proc Natl Acad Sci U S A* **115**, E9630-E9639, doi:10.1073/pnas.1809739115 (2018).
41 Ventola, C. L. Progress in Nanomedicine: Approved and Investigational Nanodrugs. *P T* **42**, 742-755 (2017).
42 Jain, K. K. in *Drug Delivery Systems* (ed Kewal K. Jain) 1-50 (Humana Press, 2008).
43 Rapamune (sirolimus) [Package Insert]. Collegeville, P., Wyeth Pharmaceuticals (2011).
44 O'Hare, F. M. *et al.* Neutrophil and monocyte toll-like receptor 4, CD11b and reactive oxygen intermediates, and neuroimaging outcomes in preterm infants. *Pediatr Res* **78**, 82-90, doi:10.1038/pr.2015.66 (2015).
45 Abbas, A. K. *Cellular and molecular immunology*. 5th edn, (Saunders, 2003).
46 Burrack, A. L., Martinov, T. & Fife, B. T. T Cell-Mediated Beta Cell Destruction: Autoimmunity and Alloimmunity in the Context of Type 1 Diabetes. *Front Endocrinol (Lausanne)* **8**, 343, doi:10.3389/fendo.2017.00343 (2017).
47 Lombardi, G. & Vasquez, Y. Dendritic cells. Preface. *Handb Exp Pharmacol*, v-ix (2009).
48 Kawamura, S. & Ohteki, T. Monopoiesis in humans and mice. *Int Immunol* **30**, 503-509, doi:10.1093/intimm/dxy063 (2018).

49 Zhu, J., Chen, H., Huang, X., Jiang, S. & Yang, Y. Ly6C(hi) monocytes regulate T cell responses in viral hepatitis. *JCI Insight* **1**, e89880, doi:10.1172/jci.insight.89880 (2016).
50 Coronel, M. M. *et al.* Immunotherapy via PD-L1–presenting biomaterials leads to long-term islet graft survival. *Science Advances* **6**, eaba5573, doi:10.1126/sciadv.aba5573 (2020).
51 Overgaard, N. H., Jung, J. W., Steptoe, R. J. & Wells, J. W. CD4+/CD8+ double-positive T cells: more than just a developmental stage? *J Leukoc Biol* **97**, 31-38, doi:10.1189/jlb.1RU0814-382 (2015).
52 Vieyra-Lobato, M. R., Vela-Ojeda, J., Montiel-Cervantes, L., Lopez-Santiago, R. & Moreno-Lafont, M. C. Description of CD8(+) Regulatory T Lymphocytes and Their Specific Intervention in Graft-versus-Host and Infectious Diseases, Autoimmunity, and Cancer. *J Immunol Res* **2018**, 3758713, doi:10.1155/2018/3758713 (2018).
53 Zhang, N. & Bevan, M. J. CD8(+) T cells: foot soldiers of the immune system. *Immunity* **35**, 161-168, doi:10.1016/j.immuni.2011.07.010 (2011).
54 Wang, C. *et al.* CD8(+)NKT-like cells regulate the immune response by killing antigen-bearing DCs. *Sci Rep* **5**, 14124, doi:10.1038/srep14124 (2015).
55 Manzoli, V. *et al.* Immunoisolation of murine islet allografts in vascularized sites through conformal coating with polyethylene glycol. *Am J Transplant* **18**, 590-603, doi:10.1111/ajt.14547 (2018).
56 Giraldo, J. A. *et al.* The impact of cell surface PEGylation and short-course immunotherapy on islet graft survival in an allogeneic murine model. *Acta Biomater* **49**, 272-283, doi:10.1016/j.actbio.2016.11.060 (2017).
57 Yi, S. *et al.* Tailoring Nanostructure Morphology for Enhanced Targeting of Dendritic Cells in Atherosclerosis. *ACS Nano* **10**, 11290-11303, doi:10.1021/acsnano.6b06451 (2016).
58 Allen, S. D., Bobbala, S., Karabin, N. B., Modak, M. & Scott, E. A. Benchmarking Bicontinuous Nanospheres against Polymersomes for in Vivo Biodistribution and Dual Intracellular Delivery of Lipophilic and Water-Soluble Payloads. *ACS Appl Mater Interfaces* **10**, 33857-33866, doi:10.1021/acsami.8b09906 (2018).
59 Yu, Y. R. *et al.* A Protocol for the Comprehensive Flow Cytometric Analysis of Immune Cells in Normal and Inflamed Murine Non-Lymphoid Tissues. *Plos One* **11**, e0150606, doi:10.1371/journal.pone.0150606 (2016).
60 Belkina, A. C. *et al.* Automated optimized parameters for T-distributed stochastic neighbor embedding improve visualization and analysis of large datasets. *Nat Commun* **10**, 5415, doi:10.1038/s41467-019-13055-y (2019).
61 Andrews, S. FastQC: a quality control tool for high throughput sequence data. *Available online at: http://www.bioinformatics.babraham.ac.uk/projects/fastqc* (2010).
62 Bolger, A. M., Lohse, M. & Usadel, B. Trimmomatic: a flexible trimmer for Illumina sequence data. *Bioinformatics* **30**, 2114-2120, doi:10.1093/bioinformatics/btu170 (2014).
63 Dobin, A. *et al.* STAR: ultrafast universal RNA-seq aligner. *Bioinformatics* **29**, 15-21, doi:10.1093/bioinformatics/bts635 (2013).
64 Trapnell, C. *et al.* Transcript assembly and quantification by RNA-Seq reveals unannotated transcripts and isoform switching during cell differentiation. *Nat Biotechnol* **28**, 511-515, doi:10.1038/nbt.1621 (2010).
65 Trapnell, C. *et al.* Differential analysis of gene regulation at transcript resolution with RNA-seq. *Nat Biotechnol* **31**, 46-53, doi:10.1038/nbt.2450 (2013).
66 Roberts, A., Trapnell, C., Donaghey, J., Rinn, J. L. & Pachter, L. Improving RNA-Seq expression estimates by correcting for fragment bias. *Genome Biol* **12**, R22, doi:10.1186/gb-2011-12-3-r22 (2011).